Combining a New 3-D Seismic S-Wave Propagation Analysis for Remote Fracture Detection with a Robust Subsurface Microfracture-Based Verification Technique

FINAL REPORT

June 6, 2000–December 31, 2003

Principal Authors: Bob Hardage, M. M. Backus, M. V. DeAngelo, R. J. Graebner, S. E. Laubach, and Paul Murray

Report Issue Date: February 2004

DOE Contract No. DE-AC26-00NT40690

Submitting Organization: Bureau of Economic Geology
The University of Texas at Austin
University Station, Box X
Austin, TX 78713-8924

Disclaimer

This report was prepared as an account of work sponsored by an agency of the United States Government. Neither the United States Government nor any agency thereof, nor any of their employees, makes any warranty, express or implied, or assumes any legal liability or responsibility for the accuracy, completeness, or usefulness of any information, apparatus, product, or process disclosed, or represents that its use would not infringe privately owned rights. Reference herein to any specific commercial product, process, or service by trade name, trademark, manufacturer, or otherwise does not necessarily constitute or imply its endorsement, recommendation, or favoring by the United States Government or any agency thereof. The views and opinions of authors expressed herein do not necessarily state or reflect those of the United States Government or any agency thereof.

Abstract

Fractures within the producing reservoirs at McElroy Field could not be studied with the industry-provided 3C3D seismic data used as a cost-sharing contribution in this study. The signal-to-noise character of the converted-SV data across the targeted reservoirs in these contributed data was not adequate for interpreting azimuth-dependent data effects. After illustrating the low signal quality of the converted-SV data at McElroy Field, the seismic portion of this report abandons the McElroy study site and defers to 3C3D seismic data acquired across a different fractured carbonate reservoir system to illustrate how 3C3D seismic data can provide useful information about fracture systems. Using these latter data, we illustrate how fast-S and slow-S data effects can be analyzed in the prestack domain to recognize fracture azimuth, and then demonstrate how fast-S and slow-S data volumes can be analyzed in the poststack domain to estimate fracture intensity.

In the geologic portion of the report, we analyze published regional stress data near McElroy Field and numerous formation multi-imager (FMI) logs acquired across McElroy to develop possible fracture models for the McElroy system. Regional stress data imply a fracture orientation different from the orientations observed in most of the FMI logs.

This report culminates Phase 2 of the study, *Combining a New 3-D Seismic S-Wave Propagation Analysis for Remote Fracture Detection with a Robust Subsurface Microfracture-Based Verification Technique.* Phase 3 will not be initiated because wells were to be drilled in Phase 3 of the project to verify the validity of fracture-orientation maps and fracture-intensity maps produced in Phase 2. Such maps cannot be made across McElroy Field because of the limitations of the available 3C3D seismic data at the depth level of the reservoir target.

Table of Contents

Disclaimer ii
Abstract iii
Introduction 1
Executive Summary 2
Experimental 3
  Geology Discussion 3
    McElroy Fracture Information 3
      Regional Stress Data 3
      Local Borehole Image Logs 4
  Geophysics Discussion 7
    Seismic Database 7
      Project History 7
      Seismic Data Acquisition 7
      Acquisition Template and Imaging Template 8
Results and Discussion 9
    Prestack Data Examples and Analyses 9
      P-Wave Data 9
      Converted-SV Data 10
    Poststack Data Examples and Analyses 13
      P-Wave Data 13
      Converted-SV Data 13
    Summary of McElroy Data Analyses 14
    Fracture-Induced S-Wave Splitting: Popular Model 16
    Popular Concepts Relating S-Wave Attributes to Fracture and Stress Properties 16
      Concept 1: S-Wave Splitting and Fracture Orientation 16
      Concept 2: Fracture Orientation and Stress Orientation 17
      Concept 3: S-Wave Splitting and Stress Orientation 18
    S-Wave Behavior When Fractures and Maximum Horizontal Stress
      Are Not Aligned 19
    S1 and S2 Traveltime Analysis: Single Interface 19
    S1 and S2 Traveltime Analysis: Dual Interfaces and Interval-Time Windows 20
    S1 and S2 Reflection Amplitudes 21
    Analysis of 3C3D Seismic Data across Fractured Carbonate Prospect Number 2 22
      Data-Acquisition Geometry 22
      Common-Azimuth Trace Gathers 23
      Interpretation of Common-Azimuth P-SV Trace Gathers 23
      Azimuth-Dependent Display of Ensemble-Average Traces 24
      Comparison of P-P and P-SV Azimuth-Dependent Properties 25
      P-SV Reflectivity Maps and Fracture Orientation 26
      Seismic-Derived and FMI-Based Fracture Orientations 27
      Confirmation of Seismic Estimation of Fracture Azimuths 28
      S1 and S2 Data Volumes 29
      S1/S2 Attribute Maps and Fracture Intensity 30
Conclusions 31
References 32
Bibliography List of Acronyms and Abbreviations 34

List of Figures

1. Regional stress map
2. Fracture planes in an elastic medium
3. FMI control wells
4. FMI fracture examples
5. Fracture orientations across McElroy Field
6. Interpreted horizontal stress pattern
7. Location map of McElroy Field
8. P-wave survey geometry
9. Converted-SV survey geometry
10. Superbin P-wave trace gather
11. Zoom view of superbin P-wave trace gather
12. Superbin trace gather of radial P-SV data
13. Superbin trace gather of transverse P-SV trace gather
14. Zoom view of radial P-SV super gather
15. Zoom view of transverse P-SV super gather
16. Superbin for analyzing azimuth-dependent P-SV properties
17. Common-azimuth displays of radial P-SV data
18. Common-azimuth displays of transverse P-SV data
19. P-P stacked data
20. P-P migrated data
21. Stacked radial P-SV data
22. Migrated radial P-SV data
23. Stacked transverse P-SV data
24. Migrated transverse P-SV data.
25. Popular fracture model
26. Dynamic fracture/stress model
27. S1 and S2 reflections, single interface
28. S1 and S2 time thicknesses across fractured intervals
29. S1 and S2 reflectivities from positive and negative impedance changes
30. Source-receiver geometry, Prospect Number 2
31. Initial analysis superbins and azimuth grid
32. Examples of S1 and S2 behavior
33. Examples of azimuth-dependent P-SV reflectivity
34. Concept of ensemble-average trace
35. Full-azimuth display format
36. Comparison of P-P and radial P-SV azimuth dependency: example 1
37. Comparison of P-P and radial P-SV azimuth dependency: example 2
38. Final superbin analysis grid
39. S1 azimuths across survey area
40. Azimuths of maximum P-SV reflectivity, Reservoir A
41. Azimuths of maximum P-SV reflectivity, Reservoir B
42. Comparisons of FMI-based and seismic-based fracture orientations
43. Crossline 60 through S1 data volume at Prospect Number 2
44. Crossline 60 through S2 data volume at Prospect Number 2
45. Inline 60 through S1 data volume at Prospect Number 2
46. Inline 60 through S2 data volume at Prospect Number 2
47. Map of S1-to-S2 reflection amplitudes from Reservoir B

Introduction

We created a geophysical and geological database across a portion of McElroy Field in West Texas for the purpose of analyzing fracture properties of a producing carbonate reservoir system. Independent seismic data-processing efforts by WesternGeco and by Bureau scientists demonstrated that the multicomponent seismic data provided by our industry partner at McElroy did not have sufficient signal-to-noise ratio to allow azimuth-dependent fracture properties to be determined.

The project was then shifted to a second fractured carbonate area where excellent quality multicomponent seismic data became available. Using this second database, we demonstrated how key fracture properties, such as azimuth orientation and relative intensity, can be estimated with multicomponent seismic data. The fracture orientation maps we developed from the multicomponent seismic data were used by the operator to drill a horizontal well that confirmed that the seismic estimates of fracture azimuth were reliable. Microfracture analyses could not be done at this second site because no oriented cores were available.

Executive Summary

The objective of this project was to combine multicomponent seismic data with a scanning-electron-microscope microfracture analysis of thin sections to develop a fracture model for carbonate reservoirs in McElroy Field in West Texas. This research objective could not be achieved because industry-provided multicomponent seismic data across McElroy Field, the principal cost-sharing contribution for the program, were found not to have adequate signal-to-noise properties to determine fracture-sensitive attributes. This conclusion is based on an extensive analysis of these McElroy multicomponent seismic data. That analysis is described in this report.

After evaluating the McElroy seismic data, the research team then deferred to an alternate fractured-carbonate study site where better quality multicomponent seismic data allowed appropriate fracture analyses to be done. No microfracture studies were done at this substitute study site because no cores were available for thin sectioning. The second half of this report uses 3C3D seismic data across this alternate study site to describe and illustrate a methodology for extracting reservoir fracture properties from multicomponent seismic data. The reliability of this methodology is then verified using data from a horizontal well that was positioned to penetrate a reservoir interval that was selected from an interpretation of seismic-based fracture-attribute maps.

Experimental

Geology Discussion

McElroy Fracture Information

Critical information about fracture properties of reservoirs can be provided by numerous measurements that do not require analyses of seismic wavefields. Two non-seismic fracture information sources that were of particular interest at McElroy Field were regional stress data and local borehole image logs.

Regional Stress Data

Zoback and Zoback (1980) discussed regional stress patterns across the United States. A portion of their map data that describes horizontal stress behavior in the McElroy area of West Texas is reproduced and modified in Figure 1. Several stress analysis sites used to construct this map are close to our study area as shown in the map inset. The real-Earth coordinates of McElroy Field will be shown later as Figure 7. The regional stress orientations for the McElroy area by Zoback and Zoback (1980) are based on hydraulic fracturing efforts in West Texas wells. The vector quantity plotted on the map at each hydrofrac test site is stated by Zoback and Zoback to be the azimuth of the *minimum* horizontal stress, which would be stress vector (σ_3) illustrated in Figure 2. The orientations of most of the vertical planes of the extensional-fracture population should be perpendicular to the azimuth of minimum horizontal stress (Fig. 2). Thus the Zoback and Zoback regional stress data imply that vertical, extensional fractures at McElroy Field should be almost east-west, or perhaps rotated to an azimuth plane about 20 degrees south of East.

Local Borehole Image Logs

An excellent database of borehole image logs was available across McElroy Field. Locations of wells where formation multi-image (FMI) logs were acquired inside the 3C3D seismic grid are shown superimposed on the seismic survey grid in Figure 3. These logs were recorded in both vertical and deviated wellbores as shown by the well symbols. Fracture analyses of these FMI data were made by a service company and also by the field operator (ChevronTexaco). We utilized the field operator's interpretations of the FMI data which we thought were a more detailed evaluation of the borehole image information.

Fracture indicators in the FMI data were segregated into two types by the field operator: high-confidence fractures and "possible" fractures. Of the total fracture indicators found in the FMI data, high-confidence fractures were less than 20 percent of the indicator population. We limited our evaluation of the McElroy fracture system to only the near-vertical, high-confidence fractures identified by the field operator. Image examples of two of these near-vertical, high-confidence fractures are shown in Figure 4.

Many geoscientists think measurements of FMI-based fracture orientations are representative of the orientation of the general fracture population penetrated by the logged well. In contrast, many of these same people believe estimates of fracture spacing and fracture width determined from FMI data may not be appropriate for extrapolating across the interwell space between FMI-imaged boreholes. Thus we limited the information that we sought from the FMI data to fracture orientation only. These local determinations of fracture azimuth would be critical for supporting, or contradicting, the

azimuth of the fast-S (S1) mode determined from 3C3D seismic data spanning the FMI-logged wells.

Azimuth orientations of near-vertical, high-confidence fractures across the seismic image space are summarized in the displays in Figure 5. All fractures used in these plots have dips greater than 80 degrees. Different fracture-orientation models develop as increasing amounts of FMI data are considered. For example, FMI log data in one well define the dominant fracture orientation to be 10 to 20 degrees south of East (left diagram), which is an orientation that agrees with the Zoback and Zoback (1980) regional stress data (Fig. 1). When FMI data from an additional eight wells are considered (center diagram), two orthogonal dominant-fracture populations develop. There is still the system of fractures oriented about 15 degrees south of East, but a larger population of fractures is now aligned 15 degrees east of North, yielding two possible fracture orientations with conflicting azimuths that differ by 90 degrees. When additional FMI data from 13 wells inside, and adjacent to, the seismic image space are considered (right diagram), the population that is 15 degrees east of North dominates the fracture orientation, a new population oriented 50 degrees east of North (and 50 degrees south of West) is the second most common occurrence, and the group oriented 15 degrees south of East that conformed to the Zoback and Zoback (1980) stress data now begins to disappear into the noise background of the orientation distribution.

One interpretation of these FMI data is that fractures in McElroy reservoirs are randomly oriented when considered over an area as large as that spanned by the FMI-log wells (about 5 km^2 [2 mi^2]). Such a medium would not produce a dominant S1 or S2

polarization of a converted-SV wavefield, which could be one reason why it was difficult to do a S1/S2 mode analysis of the McElroy 3C3D prestack data.

A second interpretation of these FMI data is that an organized and consistent fracture-to-stress model is defined as more and more high-confidence, near-vertical fractures are evaluated. To illustrate this second interpretation option, the fracture orientations expressed by the total FMI database (right diagram of Figure 5) are repeated as Figure 6. Various sectors of the fracture alignments are now labeled A, B, and C to be consistent with the stress-produced failure planes illustrated in Figure 2. This interpretation implies that a maximum horizontal stress field (σ_1) oriented about 15 degrees east of North (or 15 degrees west of South) would create essentially all of the observed fractures. Fracture population B would be extensional fractures, and populations A and C would be shear fractures (Fig. 2). This stress orientation disagrees with the Zoback and Zoback (1980) stress map (Fig. 1), which implies the orientation of the *maximum* horizontal stress would be 15 degrees south of East. These two stress interpretations (Fig. 1 versus Fig. 6) differ to the maximum possible extent in that they exchange the azimuths of the maximum and minimum horizontal stresses.

Geophysics Discussion

Seismic Database

Project History

The industry partner co-funding for this study was the cost of acquiring and processing 3C3D seismic data across a portion of McElroy Field in Crane and Upton Counties, West Texas (Fig. 7). These data were acquired by ChevronTexaco shortly before the official start date of Phase 2 of the DOE – UT contract. Bureau scientists were not involved in the seismic survey design nor in the quality control of the seismic field work. The 3C3D data were processed by WesternGeco during the early months of this Phase 2 study. The Bureau research team interacted with WesternGeco personnel during the data-processing activity and also did independent analyses of the prestack and poststack data.

Seismic Data Acquisition

Ordinarily 3C3D seismic data are acquired in a single field effort using some type of conventional P-wave energy source at the source stations and 3-component (3-C) sensors at the receiver stations. ChevronTexaco used a different data-acquisition technique at McElroy Field, with the seismic P-wave data and the converted-SV data being acquired as two separate surveys.

The P-wave data were acquired first using vertical vibrators at the source stations and vertical (only) geophones at the receiver stations. The source-receiver geometry implemented for this P-wave data acquisition is illustrated in Figure 8. Once all source stations were occupied, the vertical geophone arrays were removed, and converted-SV

data were acquired several weeks later. The P-SV data were generated using vertical vibrators at the same source stations used in the P-wave survey and were recorded using two separate sets of horizontal geophone strings at all receiver stations. Each string of geophones contained 1-component (1-C) horizontal-geophone elements. One string was deployed with its 1-C horizontal geophones oriented in the inline direction (the direction of the receiver line). A second string was then deployed with its 1-C horizontal geophones oriented in the crossline direction. The areal distribution of source and receiver stations for this converted-SV survey is illustrated in Figure 9. All receiver stations across the survey area were live as the vertical vibrators produced illuminating wavefields at each source station during both the P and converted-SV data-acquisition programs.

Acquisition Template and Imaging Template

The acquisition templates for the P-wave and converted-SV surveys were the source-receiver distributions shown in Figures 8 and 9, respectively, because all receiver stations were live for each source-station illumination. The size of the P-wave acquisition template was 4,676 m (15,340 ft) by 4,359 m (14,300 ft); the P-SV acquisition template dimensions were 2,347 m (7,700 ft) by 2,179 m (7,150 ft). The subsurface depth of the fracture target interval was only 853 to 914 m (2,800 to 3,000 ft), which requires an imaging template of approximately 1,829 m (6,000 ft) by 1,829 m (6,000 ft). The total acquisition survey for the converted-SV data thus equals only one imaging template. Generally, the dimensions of a 3-D seismic survey are several times larger than the dimensions of an imaging template. In these larger surveys, the imaging template is

moved incrementally across the survey area to build a continuous target image. No template movement was required for the McElroy survey.

Results and Discussion

Prestack Data Examples and Analyses

P-Wave Data

The signal-to-noise character of seismic field data at different imaging depths can be demonstrated by constructing prestack trace gathers. Because the geological structure across the McElroy study area was simple horizontal layering, the total acquisition template (P-wave and converted-SV) could be considered to be a single superbin. Figure 10 illustrates the result of summing the data across the entire P-wave acquisition template into a single supergather. This prestack trace gather illustrates P-wave reflection character as a function of source-to-receiver offset only. Any azimuth-dependent reflection attributes are destroyed, or modified, by the trace-summation process used to produce the gather. As many as 300 to 400 field traces, with these traces produced by a source-receiver pair oriented at a different azimuth, were sometimes summed to generate only one of the offset traces displayed in this gather.

The data window above 0.5 s that brackets the targeted fracture interval is labeled. Note that the maximum source-receiver offset for imaging this interval is 610 m (2,000 ft), which would be the lateral dimension of a good imaging template to use for the McElroy reservoirs. The maximum source-receiver offset for this particular trace gather is 1,676 m (5,500 ft), which is a little more than 70 percent of the half-width of the P-wave acquisition template (Fig. 8).

An expanded view of these prestack P-wave data across the target zone is shown in Figure 11. Even though there is reduced P-wave stacking fold at the labeled target depth, the signal-to-noise ratio of the data is good inside the targeted data window save for the nearest offset traces, which were muted during data processing. Reasonably good-quality P-wave imaging is thus achieved for the shallow reservoir target across the study area.

Converted-SV Data

A different conclusion is reached when prestack P-SV data are analyzed. The supergathers of radial and transverse P-SV data that result by summing radial and transverse components of the P-SV wavefield across the converted-SV acquisition template are displayed as Figures 12 and 13, respectively. The polarities of the radial and transverse components of the P-SV wavefield recorded in the positive-offset direction are opposite to their polarities in the negative-offset direction. Thus the polarity of negative-offset P-SV data was reversed to make the trace gathers shown in these figures. Data windows spanning the targeted reservoir interval are labeled on each display. Expanded views of the data character within the target reflection interval are shown as Figures 14 and 15. Visual comparisons of the P-wave gathers (Figs. 10 and 11) with these P-SV gathers demonstrate that the signal-to-noise ratio of the P-SV data is considerably lower than the signal-to-noise ratio of the P-wave data.

Most converted-SV energy will appear on the radial component of the scattered SV wavefield. Energy appears on the transverse component for various reasons: anisotropic properties of the propagating medium may rotate the SV particle displacement vector away from the radial plane passing through the source and receiver stations; out-of-the-

plane scatters can transfer some P-SV energy into the transverse plane; or poor geophone couplings can crossfeed radial-oriented data to the transverse geophones.

Azimuth-dependent properties of the P-SV wavefield were examined using the data-analysis template defined in Figure 16. The traces that image the interior of this superbin were segregated into trace gathers restricted to successive 10-degree azimuth corridors to determine if the arrival times of targeted reflection events varied as the orientation of the SV particle displacement vector assumed all possible azimuth-arrival directions. A sample set of common-azimuth, radial-component trace gathers is displayed in Figure 17. These data have been static-corrected, moveout velocities have been applied to flatten reflection events, and polarities have been adjusted to account for positive-offset and negative-offset domains. The diagonal line drawn across the early portion of each trace gather defines the mute boundary for that specific gather. Data to the right of this line are muted; data to the left of the line describe offset-dependent reflection arrival time and amplitude for the SV particle displacement vector that is oriented in the azimuth direction defined for each gather.

The data window that spans the reservoir interval that needs to be studied is labeled. The mute line restricts the maximum imaging offset for this target interval to about 1,097 m (3,600 ft) for each trace gather. Examination of the common-azimuth, radial-component trace gathers (Fig. 17) shows that within the reservoir interval, the inside one-third of each gather is dominated by incoherent noise, and the outside one-third has distorted wavelets caused by the interference of strong P-wave refraction events. Only the central one-third of each trace gather provides data that can be effective for target imaging and for fracture analysis of the reservoir interval, and these acceptable data have

a low signal-to-noise ratio. The end result is that reliable common-azimuth data analyses cannot be done at the target level of the McElroy reservoirs because of insufficient offset distributions, low data fold, excessive trace mute requirements, and poor signal-to-noise character at the shallow image time of this reservoir system.

Common-azimuth analysis of the transverse component of the P-SV wavefield also needs to be done when searching for S1 and S2 polarization directions. Examples of transverse-component trace gathers constructed in the same azimuth corridors as the radial-component trace gathers, and with the same static, velocity, and polarity corrections, are displayed in Figure 18. The signal-to-noise ratio of these transverse-component data is even lower than that of the radial-component data. As a result, no useful azimuth-dependent velocity or reflectivity information could be extracted from the transverse component of the P-SV data at the shallow depths of the McElroy reservoirs.

In some instances, P waves exhibit sufficient azimuth-dependent variations in arrival times (velocity) and reflectivity to allow fracture properties to be estimated. However, robust fracture analysis is better done by examining azimuth-dependent velocities and reflectivities of converted-SV data. This principle will be illustrated later in the discussion of Figures 36 and 37. Thus it was not possible to do an effective fracture analysis of the producing interval across McElroy Field using the 3C3D seismic data provided for this study because converted-SV arrival times and reflection amplitudes of both radial and transverse components of the prestack P-SV wavefield could not be analyzed in narrow-azimuth corridors. None of the prestack P-SV data allowed fast-S and slow-S arrivals, if present, to be identified.

Poststack Data Examples and Analyses

P-Wave Data

Stacking and migration are two processes that improve the signal-to-noise ratio of seismic data. Vertical slices through the stacked and migrated P-wave data volumes generated by Bureau scientists and WesternGeco, respectively, are displayed as Figures 19 and 20. These data are good quality throughout the vertical image space, including the shallow reservoir target interval. These results are not surprising considering the relatively good signal-to-noise character of the P-wave data exhibited by the prestack data (Figs. 10 and 11).

Converted-SV Data

The more critical stacked data to consider are the converted-SV data, because of the low signal-to-noise ratio exhibited by the prestack P-SV data across the fracture study interval (Figs. 12 through 15). Vertical sections through stacked and migrated data volumes of the radial-component P-SV data are shown as Figures 21 (Bureau version) and 22 (WesternGeco version). The quality of the target image in the stacked volume (Fig. 21) is surprisingly good, considering the discouraging appearance of the prestack radial-component data (Figs. 12 and 14). The image quality is slightly enhanced by migration (Fig. 22).

Vertical sections through the stacked and migrated transverse-component data volumes are displayed as Figures 23 (Bureau version) and 24 (WesternGeco version). Inspection of these data confirms what was implied by the prestack transverse-component data (Figs. 13 and 15); little usable information is provided by the transverse component

of the P-SV wavefield, not only at the reservoir level but throughout the total imaged section.

Once it is confirmed that positive-offset and negative-offset polarities are handled properly in the transverse-component stacks, there are at least two possible reasons for the lack of coherent events in the transverse-component images. One interpretation is that only minor anisotropic conditions, such as fracturing, occur within this flat-layered propagating medium to cause the converted-SV particle displacement vector to rotate away from the radial travelpath from source to receiver. A second interpretation is that anisotropic conditions exist, but these properties change so frequently in X,Y,Z space that the propagating medium behaves as a quasi-homogeneous material. In either case, the transverse component of the P-SV wavefield provides little information that can be used for fracture interpretation.

Summary of McElroy Data Analyses

The preceding commentary about the 3C3D seismic data acquired across McElroy Field, and the principles illustrated by the 3C3D data examples, can be summarized as follows:

1. To estimate fracture properties with 3C3D seismic data, the converted-SV portion of the data must be segregated into S1 and S2 subsets. This S1 and S2 segregation should be done in both the prestack and post-stack domains.
2. To make S1 and S2 data subsets, S1 and S2 polarization azimuths must first be defined. An appeal of 3C3D data is that these azimuths can be determined in the

prestack domain by interpreting common-azimuth trace gathers of radial and transverse components of the P-SV wavefield.

3. The McElroy P-SV prestack data do not have a signal-to-noise ratio across the reservoir interval that is adequate for recognizing S1 and S2 behavior in common-azimuth trace gathers.
4. Fracture analysis of the McElroy reservoirs cannot be done with these particular 3C3D seismic data.
5. The P-wave component of the 3C3D data produces a good-quality image of the McElroy reservoir interval.
6. The radial component of the P-SV wavefield produces an image of the McElroy reservoirs that may allow a limited interpretation of reservoir properties to be done with poststack converted-SV data.
7. The transverse component of the converted-SV wavefield contains no recognizable reflection events.

These observations lead to the conclusion that poststack interpretation of the McElroy 3C3D data has to be limited to analyses that integrate P-wave attributes with only a few generalized S-wave attributes, such as Vp/Vs velocity ratios, that can be created over selected data windows using the image produced with the radial component of the P-SV data. These combinations of P and S attributes can potentially distinguish some rock facies within the McElroy reservoir system, but they cannot map fracture properties reliably. Fracture-sensitive S1 and S2 data are needed for mapping fracture orientation and fracture intensity, and neither prestack nor poststack S1 and S2 data can be produced with these 3C3D data.

Fracture-Induced S-Wave Splitting: Popular Model

A seismic-based fracture model that has been widely circulated in public articles and presentations is shown in Figure 25 (Crampin, 1978, 1985, 1987; Crampin and others, 1989; Liu and others, 1989). The intent of this model has been to relate S-wave splitting phenomena to fracture orientation and to horizontal stress properties. We will first summarize some descriptions of S-wave propagation through fractured media that have been based on this model and will then point out some of the possible misuses of the model. These comments will be followed by descriptions of alternate models that can be used to apply S-wave attributes in fracture interpretations.

Popular Concepts Relating S-Wave Attributes to Fracture and Stress Properties

Concept 1: S-Wave Splitting and Fracture Orientation

The model in Figure 25 implies that an S mode that has its particle displacement vector oriented at an angle θ relative to the azimuth orientation of a system of vertical fractures will split into a fast-S mode (S1) and a slow-S mode (S2) as it propagates through the fractured interval. This model illustrates the physics of the transmitted S1 and S2 wavelets that pass through the fractured medium. Although not shown in the model, S1 and S2 wavelets also reflect from the fractured zone.

These two daughter modes, S1 and S2, that are created by S-wave bifurcation differ in two fundamental ways. First, they travel with different velocities as their names “fast” and “slow” imply. As a result, the complex wavelet that exits from the fractured interval consists of two independent, overlapped wavelets. The time delay between these two wavelets is controlled by the velocity difference between the fast and slow modes and by the thickness of the fractured interval. The difference between S1 and S2 velocities and

the thickness of the fracture propagation space must both be large for the exiting S1 and S2 wavelets to have no overlap as shown in Figure 25.

Second, the particle displacement vectors of the S1 and S2 modes are orthogonal to each other, with the S1 displacement vector being parallel to the planes of the vertical fractures and the S2 displacement vector being normal to the fracture planes. These polarization directions are indicated for the transmitted S1 and S2 wavelets in Figure 25. The same polarization relationships apply to the reflected S1 and S2 wavelets that are not shown. These distinct S1 and S2 polarization directions are caused by the difference in the mechanical strength of a system of vertical fractures in the two orthogonal directions normal to and parallel to its fracture planes, as will be discussed later. These principles are widely accepted as fundamental descriptions of the physics of S-wave propagation in fractured media.

Concept 2: Fracture Orientation and Stress Orientation

The quantity σ in Figure 25 is the horizontal stress field, with vector σ_1 indicating the azimuth of maximum horizontal stress. The basic concept implied by this model is that σ_1 is oriented in the same azimuth as the fractures (or as the dominant population of the fractures). This common assumption that fracture planes and σ_1 are aligned is not correct in some instances.

For example, Figure 2 illustrates a compressional stress field applied to an elastic medium and the strain failures that can be produced by that stress. Three distinct failure planes (fractures) may occur. One failure plane produces extensional fractures B (Fig. 2). These fractures are called tensional fractures if the minimum horizontal stress σ_3 is a tension (opposite algebraic sign to that used in Figure 2) rather than a compression

(Twiss and Moores, 1992). These extensional (tensional) fractures are indeed aligned with the maximum horizontal stress, as implied by the popular S-wave splitting model (Fig. 25). However, shear failures A and C can also be produced (Fig. 2), and they are not aligned with the maximum horizontal stress vector. The shear angle Φ varies from rock type to rock type but is skewed about 30 degrees away from σ_1 for most rocks (Twiss and Moores, 1992). Without conducting stress-strain tests on core samples under in situ conditions, it is difficult to know what percentage of the total fracture population should be assigned to fracture class B that is aligned with σ_1 and what percentages should be assigned to fracture classes A and C that are not aligned with σ_1.

Thus any model (such as Figure 25) that implies that σ_1 is aligned with fracture planes can be misleading. Such models would be correct descriptions of fracture-stress relationships *at the time of fracture genesis* if the fractures were labeled "extensional fractures" rather than just "fractures." We italicize the phrase in the preceding sentence to emphasize that the orientation of stress fields may vary over geologic time. Even though extensional (tensional) fractures and σ_1 are aligned in the same azimuth at the time of fracture genesis, tectonic processes may cause the azimuth of σ_1 to rotate away from the plane of the extensional (tensional) fractures over geologic time, as shown in Figure 26. Thus vertical fracture planes in some target intervals cannot always be assumed to be oriented in the direction of the modern-day σ_1 stress vector (Laubach and others, 2004)

Concept 3: S-Wave Splitting and Stress Orientation

A physical principle described by Figure 25 is that the S1 mode is polarized in the direction of σ_1, the maximum horizontal stress acting on the seismic propagation medium. This wave physics principle is correct when S waves propagate in a stressed, but

unfractured, medium. As a result, knowledge of S1 polarization direction infers the orientation of maximum horizontal stress in such a medium and vice versa. However, interpreters must decide what meaning should be assigned to seismic estimates of S1 azimuth in situations where the propagation medium is both stressed and fractured, and σ_1 and the fracture planes are not aligned. Possible interpretation techniques are discussed in the following sections.

S-Wave Behavior When Fractures and Maximum Horizontal Stress Are Not Aligned

Two S-wave attributes that provide valuable geologic information about fractured intervals are traveltimes and reflection amplitudes of reflected S1 and S2 modes. Integrated use of these two attributes allows interpretation of fracture properties when σ_1 and fracture planes are not aligned. A simple two-layer propagation medium will be used to illustrate the basic physics (Fig. 27).

This model is generalized to allow both S and P components of the downgoing elastic wavefield to generate S1 and S2 wavelets. The seismic data available for this DOE study were 3C3D data. Thus this discussion will focus on S1 and S2 wavelets produced by a downgoing P wavefield. This wave physics will apply to any pair of co-generated S1 and S2 wavelets (which are S1 and S2 wavelets that are produced at a common interface by a common incidence wavelet), whether the wavelets are produced by a downgoing P wavefield or by a downgoing S wavefield.

S1 and S2 Traveltime Analysis: Single Interface

A key concept illustrated in Figure 27 is that the time delay between upgoing co-generated S1 and S2 reflection events is produced as these wavelets travel through the

overburden above a fracture target. Thus any traveltime-based analysis of co-generated S1 and S2 wavelets describes S-wave splitting phenomena associated with the overburden, not with the fracture target that produced the reflections. In particular, the upgoing S1 event that arrives at a surface-positioned sensor will be polarized in the azimuth of the maximum horizontal stress in the overburden as discussed in *Concept 3: S-Wave Splitting and Stress Orientation*.

If the maximum horizontal stress field in the overburden is aligned with the fracture planes in the underlying fractured interval, then traveltime-based analyses of S1 and S2 polarizations can be used to interpret fracture orientation in a fractured target beneath a stressed overburden. However, if σ_1 within the overburden is not aligned with fracture azimuth, then traveltime-based analyses of co-generated S1 and S2 wavelets should not be used to interpret fracture orientation in a unit beneath a stressed overburden. Such analyses determine only the azimuth of σ_1 within the overburden unless the analysis is restricted to an interval analysis of S1 and S2 images across a thin seismic window that brackets a fracture target, as will be discussed in the next section.

Using traveltime-based analysis of co-generated S1 and S2 wavelets in fracture interpretation, without consideration of possible misalignments of the azimuths of σ_1 and the fracture planes, is one of the common misuses of the model in Figure 25.

S1 and S2 Traveltime Analysis: Dual Interfaces and Interval-Time Windows

S1 and S2 traveltime analyses can provide valuable fracture information if the analyses are restricted to the depth interval that spans only the fracture space. The dual-interface Earth model in Figure 28 is a modification of the single-interface model in Figure 27. In this latter model, the fracture space is bounded by two S1/S2 reflecting

boundaries, A and B. The symbol T represents seismic traveltime from a specified interface, and ΔT is the interval traveltime between interfaces A and B.

The point emphasized in the preceding section is that an analysis of T(S1) or T(S2) from only interface A or from only interface B will provide information about the azimuth of σ_1 within the overburden above the fracture space but no information about fracture properties within the fractured interval. In contrast, interval traveltimes ΔT(S1) and ΔT(S2) that utilize two sets of co-generated S1 and S2 wavelets, one set from interface A and one set from interface B, provide information describing S-wave velocity behavior strictly across the fracture space. Information about the overburden is eliminated by the subtraction process used to estimate ΔT across the target interval (Fig. 28). This interval-time technique will be used to generate fracture intensity maps in the discussion of Prospect Number 2 at the close of this report.

S1 and S2 Reflection Amplitudes

The lithofacies unit overlying a fractured interval can have a seismic impedance greater than or less than the seismic impedance within the fractured facies. The S1 and S2 modes that reflect from the fractured interval have opposing azimuth-dependent behaviors in these two impedance-contrast situations. The reflectivity principles are summarized in Figure 29.

In most cases, rock units that bound a fractured interval are “softer” than the fractured facies and have an S-wave elastic impedance that is lower than the S-wave impedance within the fractured lithofacies. Thus the S-wave reflectivity behavior labeled “Case 1” in Figure 29 will be the more common situation that will occur at the upper interface of a fractured target.

Analysis of 3D3C Seismic Data across Fractured Carbonate Prospect Number 2

Because the signal-to-noise ratio (S/N) of the 3C3D seismic data at the shallow depths of the targeted reservoirs at McElroy Field was too low for a reliable analysis of azimuth-dependent P-SV data properties to be done, we deferred to an alternate 3C3D seismic survey acquired across a different carbonate reservoir to illustrate how 3C3D data can assist the characterization of fracture systems. This new study area will be referred to as Prospect Number 2.

At this alternate prospect, there are two fractured carbonate reservoirs, separated vertically about 152 m (500 ft), that drape over an anticlinal structure inside the seismic image space. Reservoir depths average about 2,000 m (6,562 ft) across the imaged structural relief.

Data-Acquisition Geometry

The source-receiver geometry used to acquire the 3C3D data at Prospect Number 2 is shown in Figure 30. Receiver lines 1, 2, 3 were oriented northeast-southwest; receiver lines 4, 5, 6 were laid out northwest to southeast. Receiver line spacing was 1,000 m (3,281 ft). Receiver stations were spaced at intervals of 50 m (164 ft). A 3-element array of 3-component geophones was deployed at each receiver station, with the three geophones at each station separated only 1 m (3 ft) or less to create a point receiver that would not be affected by intra-array static variations.

The energy source was 2 kg of high-velocity explosive (Simigel) positioned at a depth of 9 m (30 ft). Shotholes were randomly distributed across the survey area as shown in Figure 30.

Common-Azimuth Trace Gathers

Radial P-SV trace gathers were produced over superbins of various sizes to optimize the signal-to-noise ratio (S/N) of the gather data. One example of a set of nine test superbins is shown in Figure 31. Each of these superbins encompasses an area of 19 × 19 standard stacking bins. Overlapping 9 × 9 superbins were used in the final data analysis.

Azimuth grids were positioned on each superbin to create common-azimuth P-SV trace gathers needed for fracture analysis. One grid used to make trace gathers in 30-degree azimuth ranges is shown in Figure 31. Subsequent grids created trace gathers in which the azimuth increment was reduced to 20 degrees.

Interpretation of Common-Azimuth P-SV Trace Gathers

An example of S-wave splitting information provided by common-azimuth P-SV trace gathers is shown in Figure 32. These gathers of the radial component of the P-SV wavefield were made in the center superbin of Figure 31 and confirm that there is a significant difference in the P-SV reflection times from the targeted reservoirs A and B when the P-SV wavefield travels in different azimuth directions. At this superbin location, the earliest reservoir reflection times occur in the 30 – 60 degree azimuth corridor; the latest reflection times are in the 120 – 150 degree azimuth range. The interpretation is that, at this superbin location, the S1 mode is polarized at an azimuth of approximately 45 degrees (the center of the 30 – 60 degree azimuth corridor), the S2 mode is polarized in an azimuth of about 135 degrees, and there is about a 50-ms time delay between the S1 and S2 reflections.

A second radial P-SV trace gather example is shown in Figure 33. This trace gather was created in superbin 3 in Figure 31 and confirms that P-SV reflection amplitude from

the fractured reservoirs also varies with the azimuth at which the P-SV wavefield travels. This phenomenon, azimuth variation of P-SV reflectivity, will be used to construct a seismic-based estimate of fracture orientation across the prospect.

To infer fracture information from P-SV reflection data, it is necessary to devise a convenient and robust methodology for displaying and interpreting the azimuth dependency of P-SV reflection times and amplitudes of targeted fractured units. The technique used in this instance was first to create common-azimuth trace gathers (such as Figs. 32 and 33) and then to sum each trace gather over an appropriate offset range to form a single trace that summarized the P-SV reflection time and amplitude behavior within that azimuth corridor.

Care must be used when summing a trace gather into a single trace that represents the reflection time/amplitude character of the trace-gather ensemble because of the large variations in reflection waveshape that occur across offset space. Our approach was to sum the common-azimuth trace gathers over a restricted offset range where there was a reasonable consistency in reflection phase and amplitude. Restricted-offset data windows such as the one illustrated in Figure 34 were used to construct an ensemble-average trace for each common-azimuth trace gather.

Azimuth-Dependent Display of Ensemble-Average Traces

An example of a full-azimuth display of ensemble-average traces is shown in Figure 35. In each 20-degree azimuth corridor, the ensemble-average trace is repeated three times to allow better visualization of reflection arrival times and amplitudes as the 20-degree corridor is rotated around the 180-degree azimuth range from North to South.

This display focuses on the radial P-SV reflections from targeted fracture reservoirs A and B as observed in a stacking bin at the center of the data-acquisition grid. Inspection of the figure shows that the arrival times of the radial P-SV reflections vary with azimuth, and equally important, the amplitudes of the reservoir reflections also vary with azimuth.

Comparison of P-P and P-SV Azimuth-Dependent Properties

We created common-azimuth gathers of reflected P-P data also to determine if P-P reflection wavefields from the fracture reservoirs exhibited azimuth-dependent properties that could be used to infer orientations of rock anisotropy axes, as can azimuth variations of reflected P-SV data (Figs. 32, 33, and 35).

Our investigation showed that P-P reflections from the targeted reservoirs exhibited much smaller azimuth variations in arrival time and reflection amplitude than converted-SV reflections. An example of the most common P-P behavior observed across the seismic image space is illustrated in Figure 36. Compared to the azimuth-dependent arrival times and reflectivities exhibited by the radial P-SV data in this same analysis bin, reflected P-P data exhibit small sensitivities to rock anisotropy. The largest P-P azimuth-dependent behavior found across the entire seismic image space is illustrated as Figure 37. At this analysis bin, P-P arrival time (velocity) in the slow-S polarization direction exhibited its maximum time delay. However, the variation in P-SV arrival time (about 50 ms) is an order of magnitude larger than the azimuth variation in P-P arrival time (about 4 ms) and is thus a more robust parameter for interpreting azimuth orientations of rock-anisotropy axes.

In summary, common-azimuth P-P trace gathers did not provide significant information about rock anisotropy at this particular prospect, whereas P-SV trace gathers

provided strong indications of rock anisotropy. This conclusion should not be used as a universal rule. There will be some seismic propagation media where P-P data, properly analyzed, can be an important asset for interpreting orientations of anisotropy planes and rock-symmetry axes.

P-SV Reflectivity Maps and Fracture Orientations

Common-azimuth radial P-SV trace gathers were generated at 192 superbins across the seismic test grid illustrated in Figure 30. Each superbin measured 225 m (738 ft) by 225 m (738 ft) (9 standard bins × 9 standard bins). The centerpoints of successive bins were displaced 125 m (410 ft) (5 standard bins) in the inline and crossline directions to create a 100-m (328-ft) (4-bin) overlap from superbin to superbin. These superbins were clustered in the highest P-SV stacking folds produced by the acquisition grid (Fig. 38).

The radial P-SV trace gather information generated at each superbin was summarized into the ensemble-trace format illustrated in Figure 35 for fracture analysis. The objective of the data interpretation was to determine the azimuth of maximum radial P-SV reflectivity from the fractured reservoirs at each superbin location. The azimuth in which this maximum radial P-SV reflectivity occurred was then assumed to define the azimuth of the vertical fracturing within the targeted reservoir at the superbin location (Fig. 29). The azimuth of S1 polarization was also interpreted at each superbin to determine the areal pattern of maximum horizontal stress within the overburden above the fracture target.

Maps of the azimuth variations of S1 polarization, maximum radial P-SV reflectivity from Reservoir A, and maximum radial P-SV reflectivity from Reservoir B are shown in

Figures 39, 40 and 41, respectively. The P-SV maximum reflectivity map for each reservoir is assumed to be a fracture-azimuth map for that reservoir.

Seismic-Derived and FMI-Based Fracture Orientations

A FMI (Formation Multi-Imager) log was recorded over Reservoir B in the vertical portion of the well labeled C1 in Figure 41. The horizontal portion of this well was drilled before the 3C3D seismic test data were acquired. ResTech analyzed the FMI data for the field operator and created a plot of the azimuth distributions of the near-vertical fractures observed over the reservoir interval. These log-based fracture azimuths are compared with azimuths of radial P-SV maximum reflectivities in Figure 42. The P-SV maximum reflectivity occurred in an azimuth corridor of 20 – 40 degrees east of North at all superbins immediately around the C1 well. The midpoint value of 30 degrees for this azimuth corridor approximated closely the average azimuth of the FMI-based fracture orientations as can be seen in the illustration.

The fast-S polarization direction at each superbin was assumed to define the azimuth of the maximum horizontal stress acting on the overburden above the fractured reservoirs at that superbin location. Reduced data quality did not allow valid S1/S2 azimuths or P-SV reflectivities to be determined near major faults. Prestack depth migration would probably have allowed valid trace gathers to be constructed along the fault trends, but we did not have access to computational resources that could produce prestack depth-migrated data.

The key conclusion reached in this study was that converted-SV data having adequate signal-to-noise character, when properly processed and interpreted, can be a reliable technology for detecting and mapping fracture orientations.

Confirmation of Seismic Estimation of Fracture Azimuths

There is anecdotal confirmation that the fracture orientations implied by the maps in Figures 40 and 41 are correct. Using these "fracture orientation" maps, the field operator drilled a horizontal well that started near the C1 well (Figs. 40 and 41) and trended southeast through Reservoir B so the wellbore would be perpendicular to the azimuths of the maximum P-SV reflectivity azimuths observed in the seismic analysis. This drilling direction should cause the wellbore to penetrate the largest possible number of independent fractures.

Log data from that well were not provided to the research team. However, the operator made two observations to our research team about the drilling results that are significant. First, the operator concluded that the orientations of the near-vertical fractures observed in the wellbore agreed, within error bounds acceptable to that operator, with the fracture orientations shown by the seismic-derived fracture azimuth map (Fig. 41). This finding, though not substantiated by hard data, is offered as documentation that common-azimuth analyses of reasonable quality P-SV data can infer fracture orientation.

Second, the operator found that the well did not produce hydrocarbons at attractive flow rates because many of the intersected fractures were filled with cement and had low permeabilities and storage volumes. Because of this finding, the 3C3D seismic data were then analyzed to determine if S1/S2 interval transit times could be used as discussed in

Figure 28 and if S1/S2 amplitudes could be analyzed as described in Figure 29 to indicate spatial variations of fracture intensity and openness.

S1 and S2 Data Volumes

A key objective of prestack common-azimuth data analysis is to determine S1 azimuth in the overburden above a fractured target so 3C3D seismic data can then be rotated to position the radial and transverse components of the converted-SV wavefield in the azimuths of the principal stress axes in the overburden. An average S1 azimuth across the seismic image space at Prospect Number 2 was determined using the map in Figure 39. The 3C3D field data were then rotated to position the radial P-SV component in this S1 azimuth, causing the transverse P-SV component to be in the S2 azimuth. The radial-component and transverse-component P-SV data were then processed as two separate data sets to produce a S1 and a S2 data volume, respectively.

Vertical slices through the migrated S1 and S2 volumes are shown as Figures 43 through 46. Fractured reservoirs A and B are labeled in each display. Three horizons are shown that track key phases of the reflection event from each fractured-carbonate interval, A and B. These horizons can be used to determine S1 and S2 attributes that can then be combined to estimate fracture intensity in each reservoir, Comparing Figure 43 with 44 and Figure 45 with 46, each of the S2 horizons is delayed by approximately 50 ms compared with its S1 equivalent. The S2 image also shows that Reservoir A and Reservoir B reflection events exhibit weaker amplitudes at some image coordinates than what is observed in the S1 image.

S1/S2 Attribute Maps and Fracture Intensity

Popular fracture-intensity interpretation models utilize various combinations of S1 and S2 seismic attributes. A model based on ratios of S1 and S2 interval transit times and another based on ratios of S1 and S2 reflection amplitudes are illustrated in Figures 28 and 29, respectively. An application of a reflection amplitude model for Reservoir B is illustrated by the map displayed in Figure 47, which shows lateral variations of the ratio of S1-to-S2 reflection amplitudes for Reservoir B across the seismic image space.

The ratio of S1:S2 reflection amplitudes should never be less than 1.0 if the layer above the fractured interval has an S-wave impedance less than the S-wave impedance of the fracture zone (Case 1, Figure 29). Log data provided to the research team across Prospect 2 imply that the assumption of a Case 1 type fracture model can be applied to these data. This assumption seems to be verified by the amplitude ratios in Figure 47, which have magnitudes greater than 1.0.

The S1:S2 amplitude ratio must be viewed as a *qualitative* indicator of fracture content within an interval, not as a *quantitative* indicator. Higher ratio values indicate increased fracture content within the interval that generated S1/S2 reflection events, but it is not possible to assign numerical fracture-content magnitudes to a ratio value. The map in Figure 47 implies that within Reservoir B, fracture content is greatest along a corridor (blue colors) immediately southeast of the northeast-southwest-trending fault that traverses the image space and along a corridor (again blue colors) trending northwest-southeast between inline coordinates 30 and 40. An area of decreased fracture content is implied by the red colors bounded by inlines 60 to 90 and crosslines 40 to 60. The amplitude ratios in the blue corridors and in this red area differ by a factor of 2, but

extensive subsurface data will be required to determine the magnitude of the differences in the actual fracture content of Reservoir B across these areas. For the present, our interpretation has to be limited to the idea that the map in Figure 47 indicates only relative variations in fracture intensity. Assigning fracture intensity numbers to this ratio map, or to any map based on S1 and S2 seismic parameters, requires expanded databases and further research.

Conclusions

Our effort to detect and map fracture properties across McElroy Field in Crane and Upton Counties, West Texas, had to be abandoned because industry-provided 3C3D seismic data needed for the study did not allow azimuth variations of converted-SV reflections to be analyzed at the shallow depths of the targeted reservoir. Considerable project time elapsed before the research team was forced to conclude that the McElroy seismic data would not create an acceptable multicomponent database for characterizing fracture systems within McElroy Field.

A second 3C3D seismic survey, acquired by a different industry operator across an alternate fractured carbonate reservoir, was then used to document the value of converted-SV data in analyzing fractured rock systems. The shift of project emphasis to this substitute 3C3D seismic survey allowed important fracture-sensitive seismic analysis techniques to be illustrated. The key principles that we documented were:

1. When a seismic propagation medium has a reasonable amount of anisotropy, converted-SV wavefields bifurcate into fast-S (S1) and slow-S (S2) modes.

2. S1 and S2 azimuths can be estimated in the prestack domain by creating common-azimuth trace gathers of radial and transverse components of the reflected P-SV wavefield.
3. Azimuth-dependent variations in propagation velocity and/or reflectivity are greater for P-SV reflected data than for P-P reflection data.
4. Fracture orientation coincides with the azimuth in which there is the maximum reflectivity of the radial component of the P-SV wavefield. This concept was verified by well control at Prospect Number 2.
5. Using prestack determinations of S1 and S2 azimuths, 3C3D data can be processed to generate independent S1 and S2 data volumes.
6. Attributes extracted from S1 and S2 data volumes can be used to infer key fracture properties, such as fracture orientation and relative fracture intensity.
7. The ratio of S1-to-S2 reflection amplitudes indicated where fracture intensity for one targeted reservoir interval increased and decreased in a relative sense. This concept was supported by anecdotal information provided by the field operator.

References

Crampin, S., 1978, Seismic wave propagation through a cracked solid: polarization as a possible delatancy diagnostic: Geophys. J. Roy. Astr. Soc., v. 53, p. 467–496.

Crampin, S., 1985, Evidence for aligned cracks in the earth's crust: First Break, v. 3, p. 12–15.

Crampin, S., 1987, Geological and industrial implications of extensive-dilatancy anisotropy: Nature, v. 328, p. 491–496.

Crampin, S., Lynn, H. B., Booth, D. C., 1989, Shear-wave VSPs: a powerful new tool for fracture and reservoir description: J. Petrol. Tech., v. 41, no. 3, p. 283–288.

Laubach, S. E., Olson, J. E., Gale, J. F. W., 2004, Are open fractures necessarily aligned with maximum horizontal stress?: Earth and Planetary Science Letters (in press).

Liu, E., Crampin, S., Booth, D. C., 1989, Shear-wave splitting in cross-hole surveys: modeling: Geophysics, v. 54, p. 57–65.

Twiss, R. J. and Moores, E. M., 1992, Structural geology: W. H. Freeman and Company, New York, 532 p.

Zoback, M. L., and Zoback, M., 1980, State of stress in the conterminous United States: J. Geophys. Research, v. 85, no. B11, p. 6113–6156.

Bibliography List of Acronyms and Abbreviations

Co-generated S1/S2 wavelets:	S1 and S2 wavelets produced at a common interface by a common incidence wavelet
Converted-SV:	An upgoing SV shear mode produced when a downgoing P-wave mode arrives at an interface at a nonvertical angle of incidence
FMI:	Formation Multi-Imager log
Negative offset:	That direction away from a source station in which a converted-SV particle-displacement vector has a negative polarity
Positive offset:	That direction away from a source station in which a converted-SV particle-displacement vector has a positive polarity
P:	Compressional mode of a seismic wavefield
P-SV:	A converted-SV mode
SV:	Vertical shear wave mode of a seismic wavefield
S1:	The fast-S shear wave mode
S2:	The slow-S shear wave mode
3C3D:	Three component and three dimensional

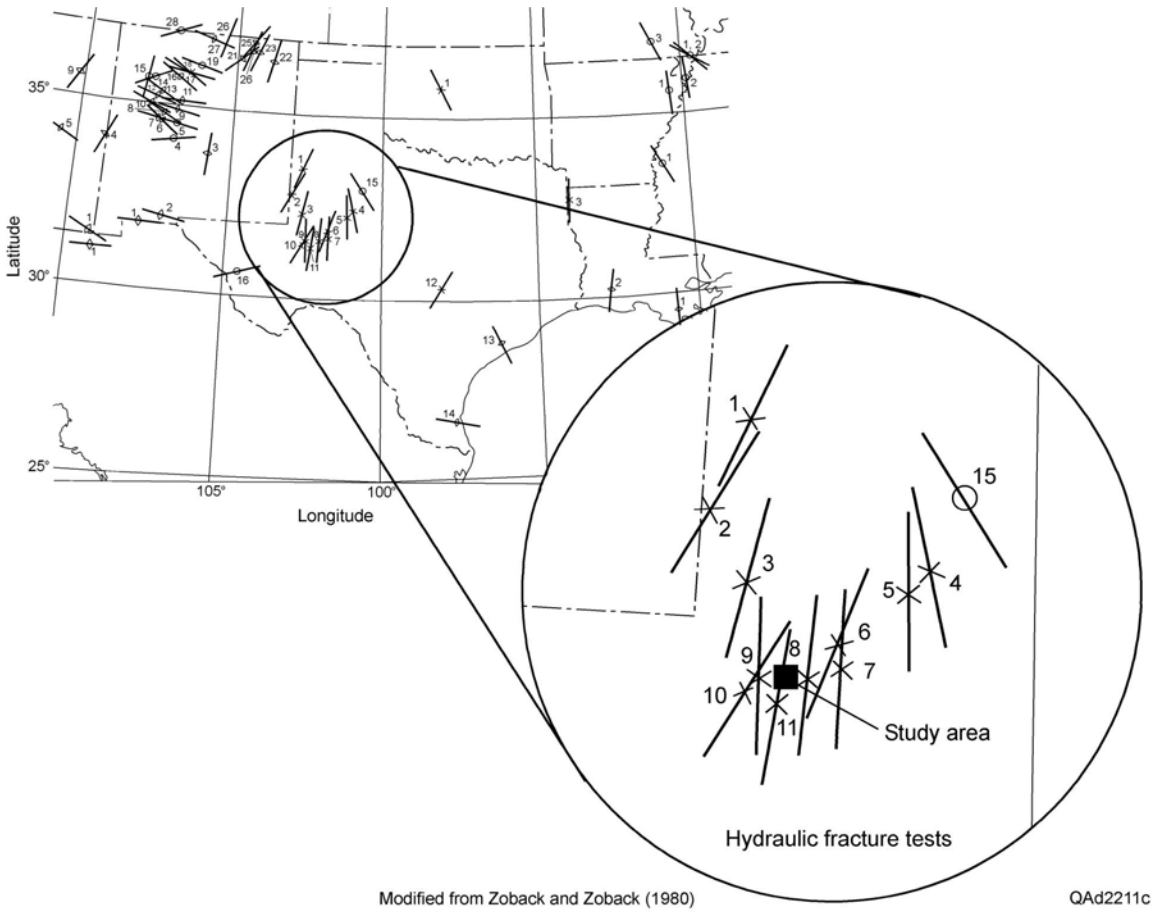

Figure 1. Regional stress data map from Zoback and Zoback (1980). The location of the McElroy project study area is indicated in the zoom view. Zoback and Zoback defined the orientations of the plotted lines as the azimuths of minimum horizontal stress. Each numbered test site was a well where hydraulic fractures were induced in the formation. Vertical extensional fractures should be normal to these minimum-horizontal-stress vectors.

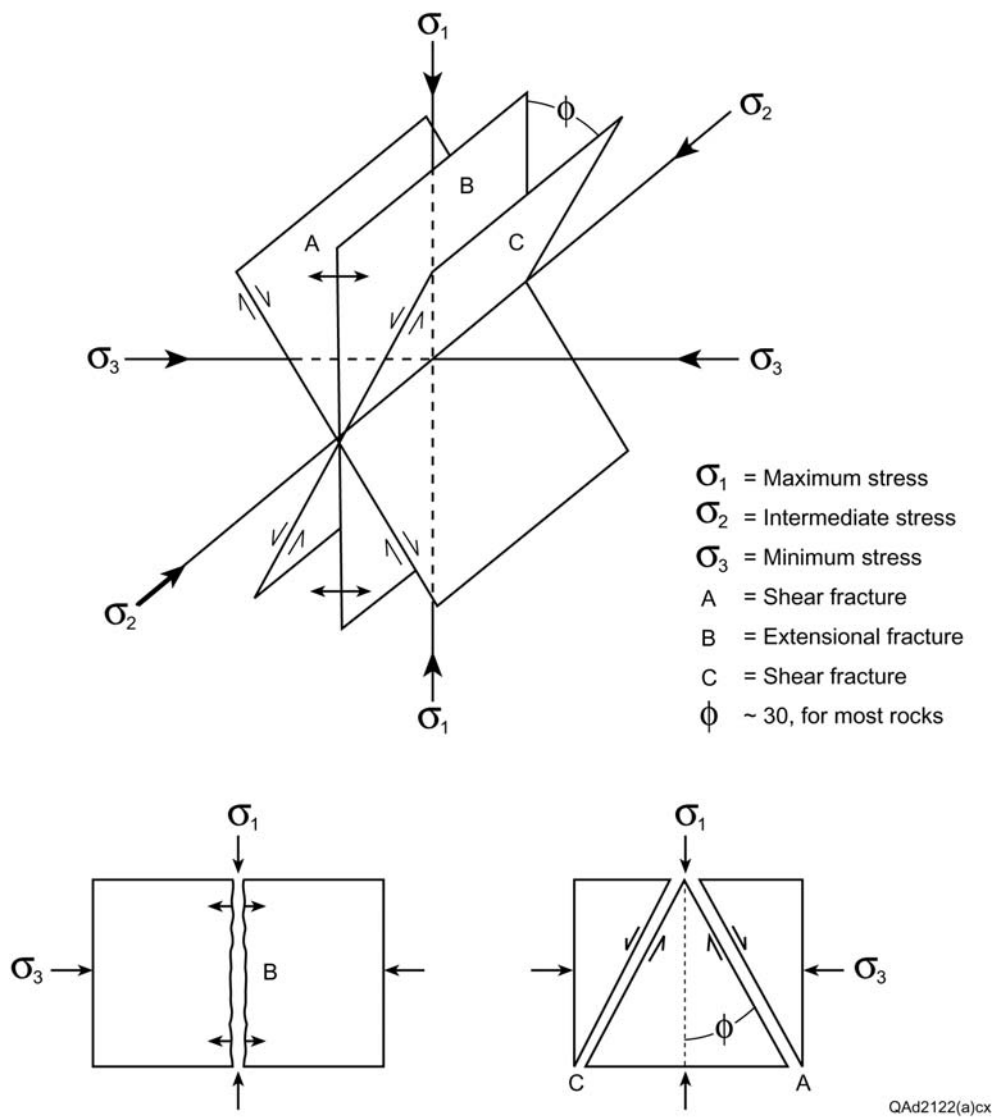

Figure 2. Fracture planes caused by compressive stress failure of an elastic medium. Fracture B is an extension fracture if σ_3 is compression (as shown) and is a tension fracture if σ_3 is tensile (opposite to the vector direction shown in the diagram).

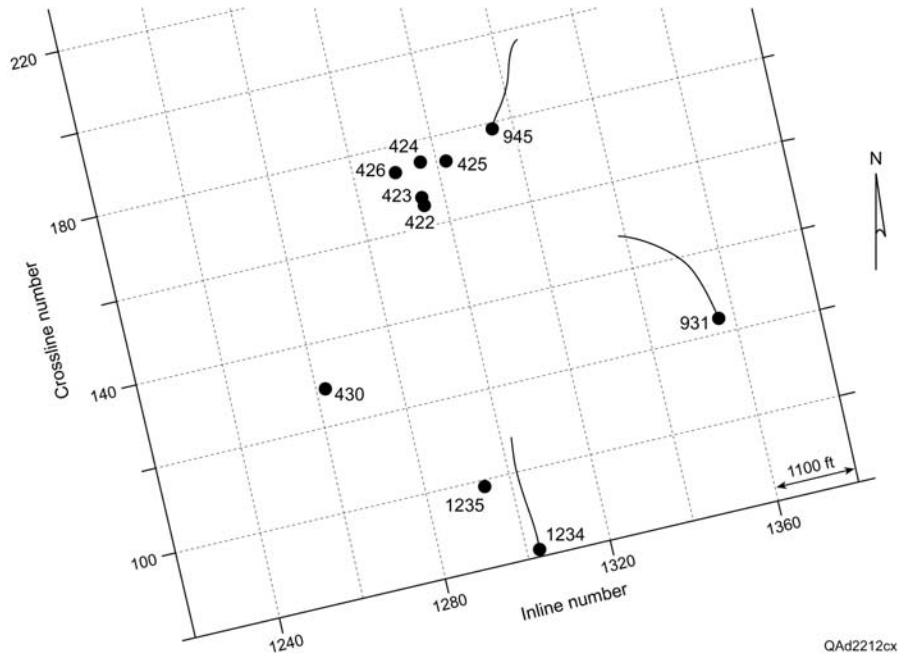

Figure 3. Wells within the seismic image space at McElroy Field where Formation Multi-Image (FMI) log data were acquired. Wells 931, 945, and 1234 were deviated boreholes.

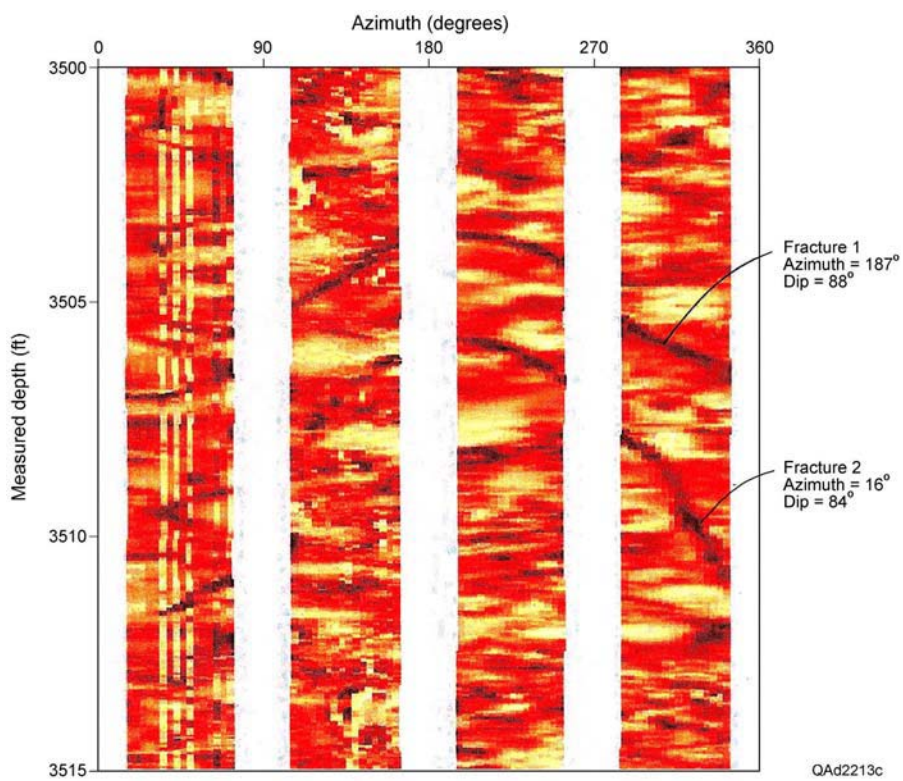

Figure 4. FMI data acquired in well 931 showing examples of two high-confidence, near-vertical fractures interpreted by the operator of McElroy Field.

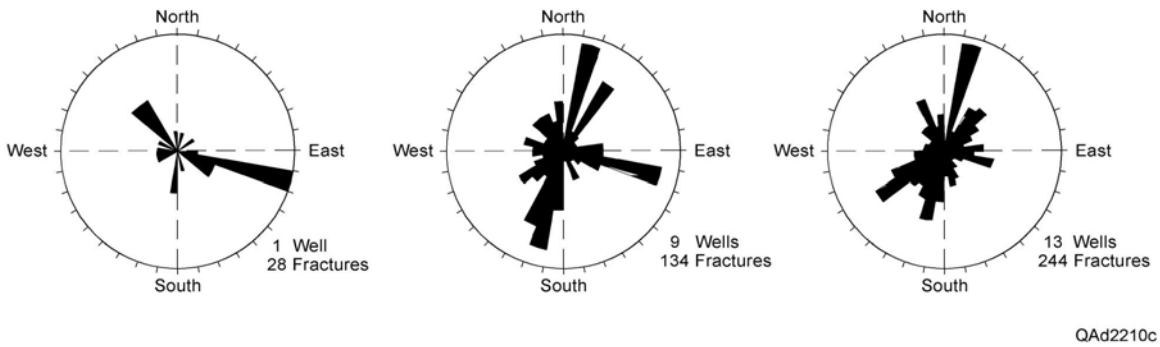

Figure 5. Orientations of high-confidence, near-vertical fractures across McElroy Field. The length of the trend plotted in any azimuth direction is proportional to the number of fractures oriented in that azimuth corridor. The left diagram summarizes the FMI data analysis in well 931. The center diagram depicts FMI interpretations in wells 224hL, 224hu, 423, 424, 425, 426, 430, 844h, and 931, which are inside, or immediately next to, the seismic image space. The right diagram summarizes FMI interpretations from these nine wells and from four other wells in the immediate area.

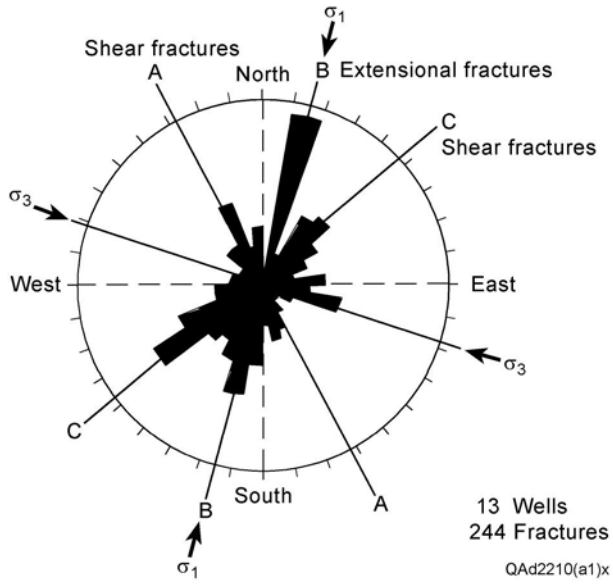

Figure 6. Possible horizontal-stress pattern interpreted from McElroy FMI fracture orientations. Fracture populations A, B, C (shear, extension, shear) and horizontal stresses σ_1 and σ_3 are defined in Figure 2.

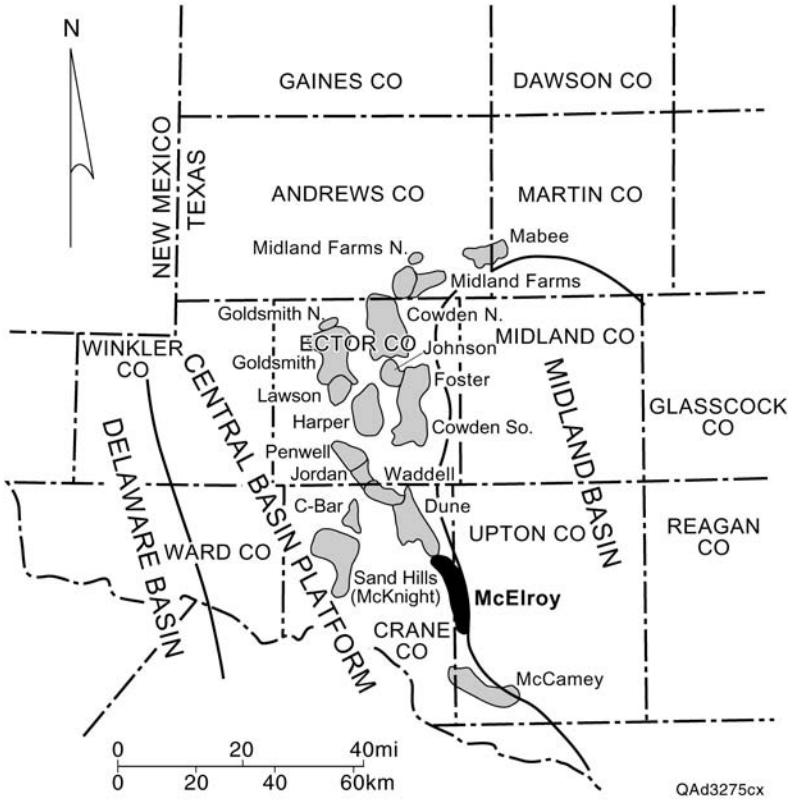

Figure 7. Location map for McElroy Field.

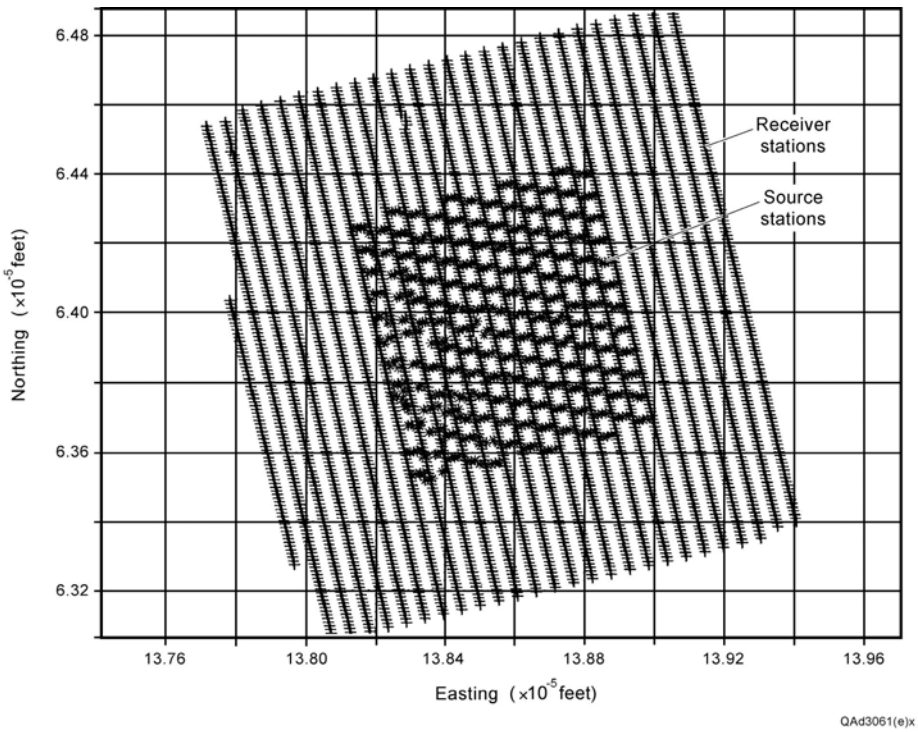

Figure 8. Survey geometry used to acquire the 3-D, 1-component, P-wave data.

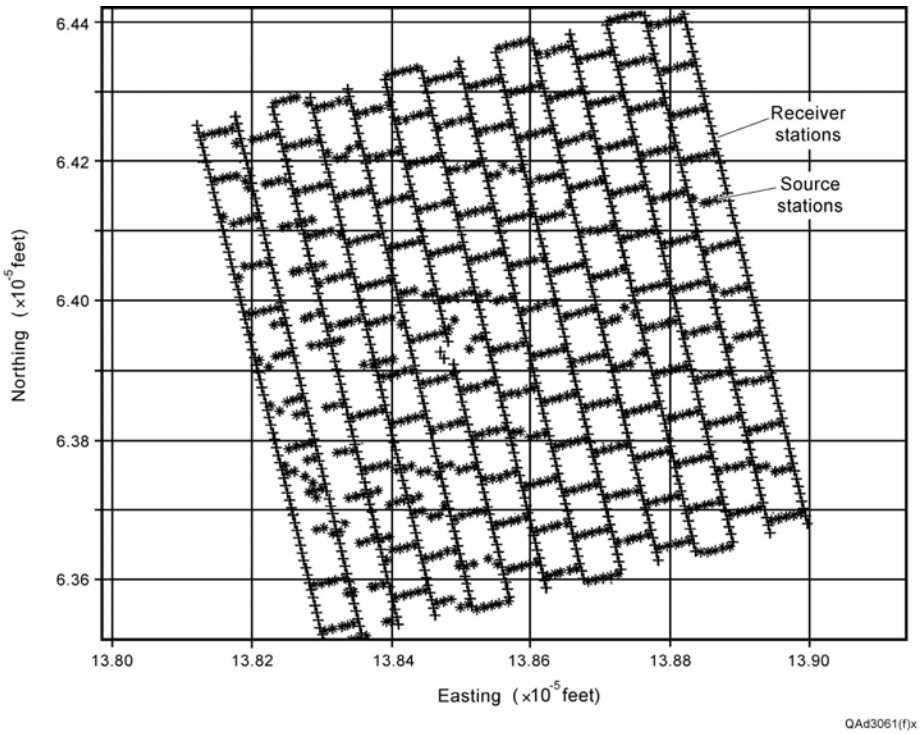

Figure 9. Survey geometry used to acquire the 3-D, 2-component, converted-SV data.

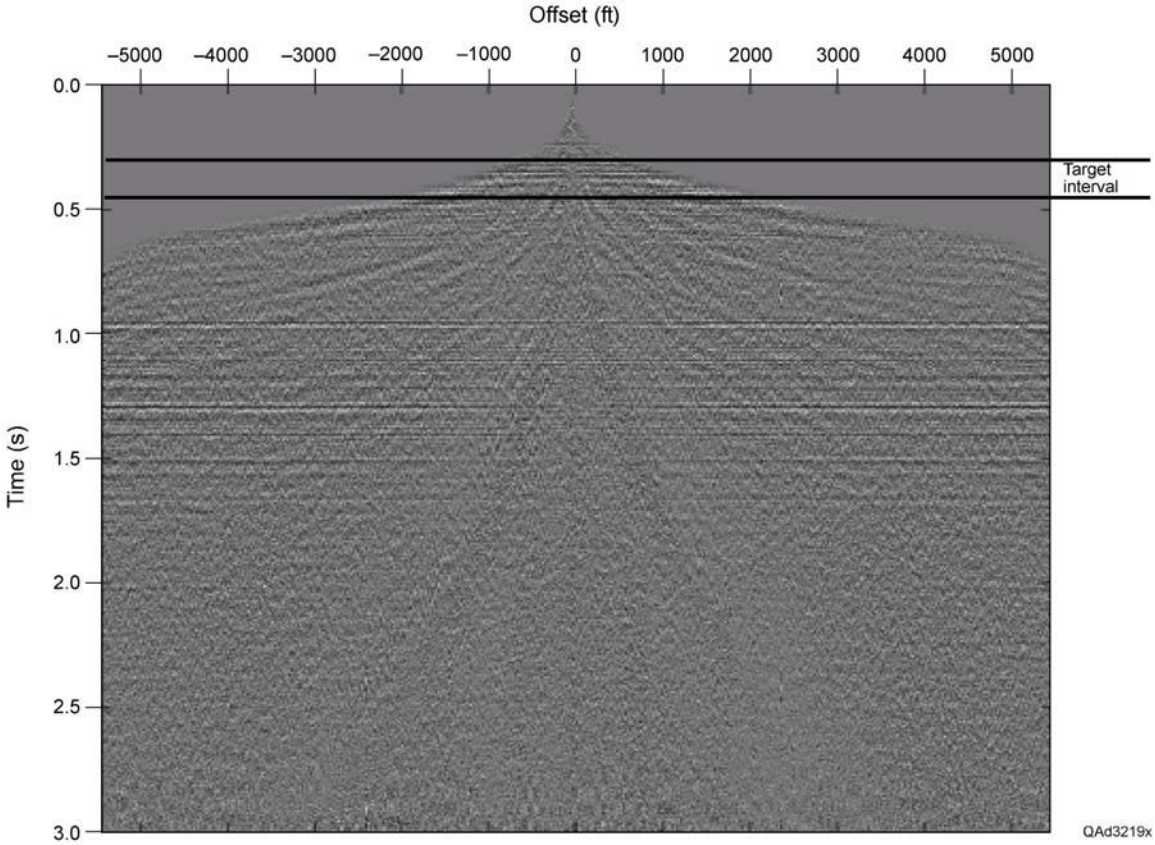

Figure 10. Superbin P-wave trace gather. The target interval for the McElroy reservoir facies is labeled.

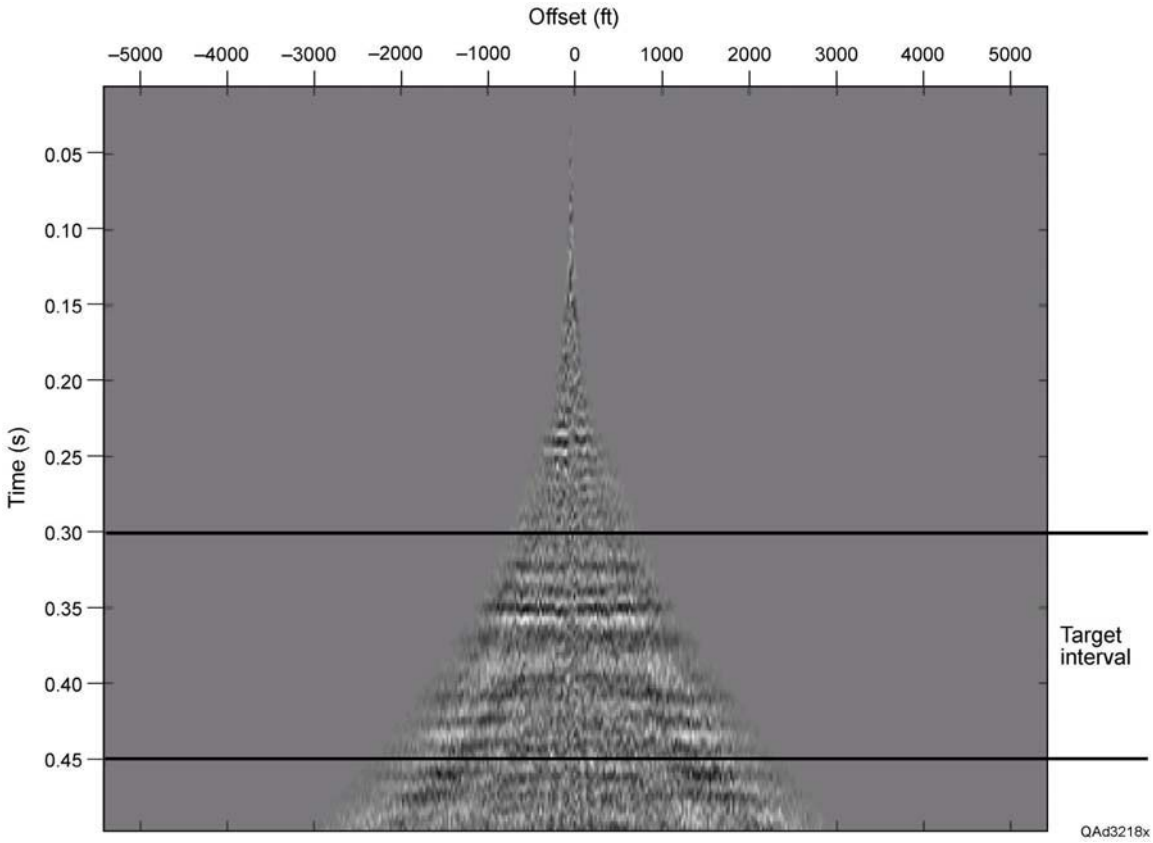

Figure 11. Zoom view of superbin P-wave events that image the targeted reservoir interval.

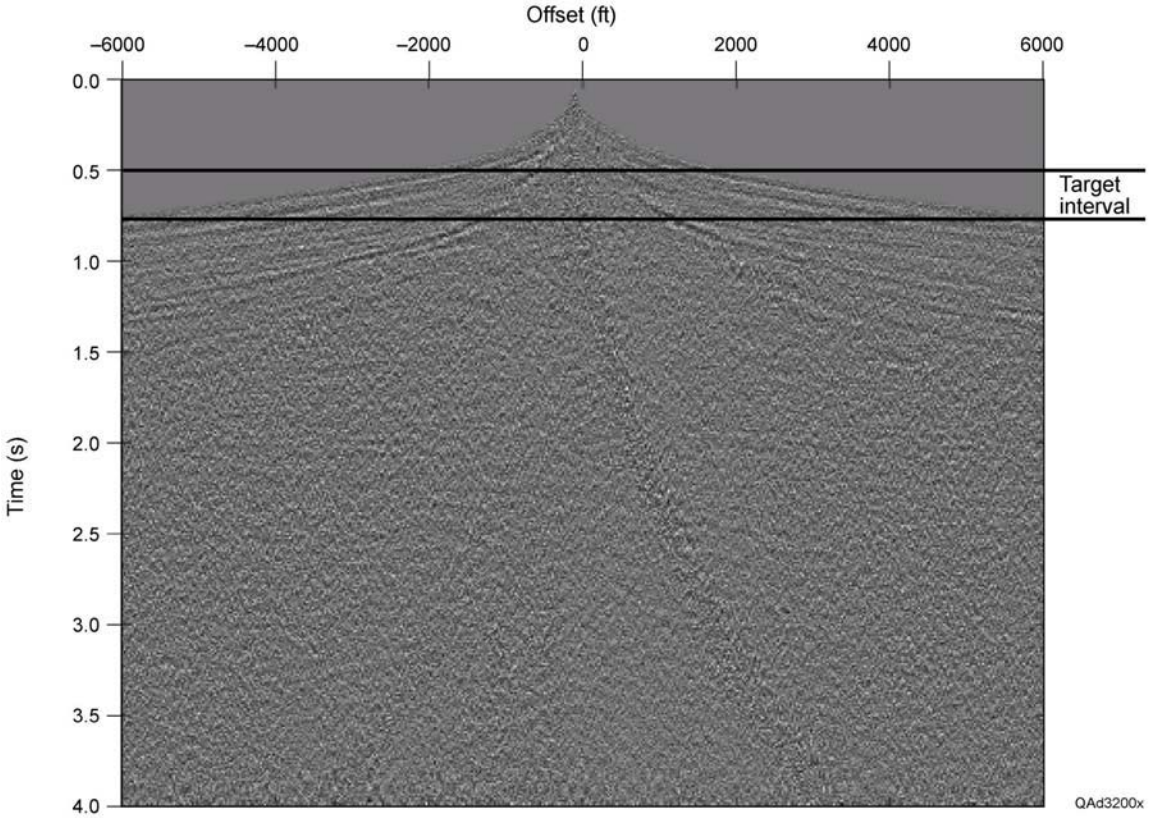

Figure 12. Superbin trace gather of the radial component of the converted-SV wavefield.

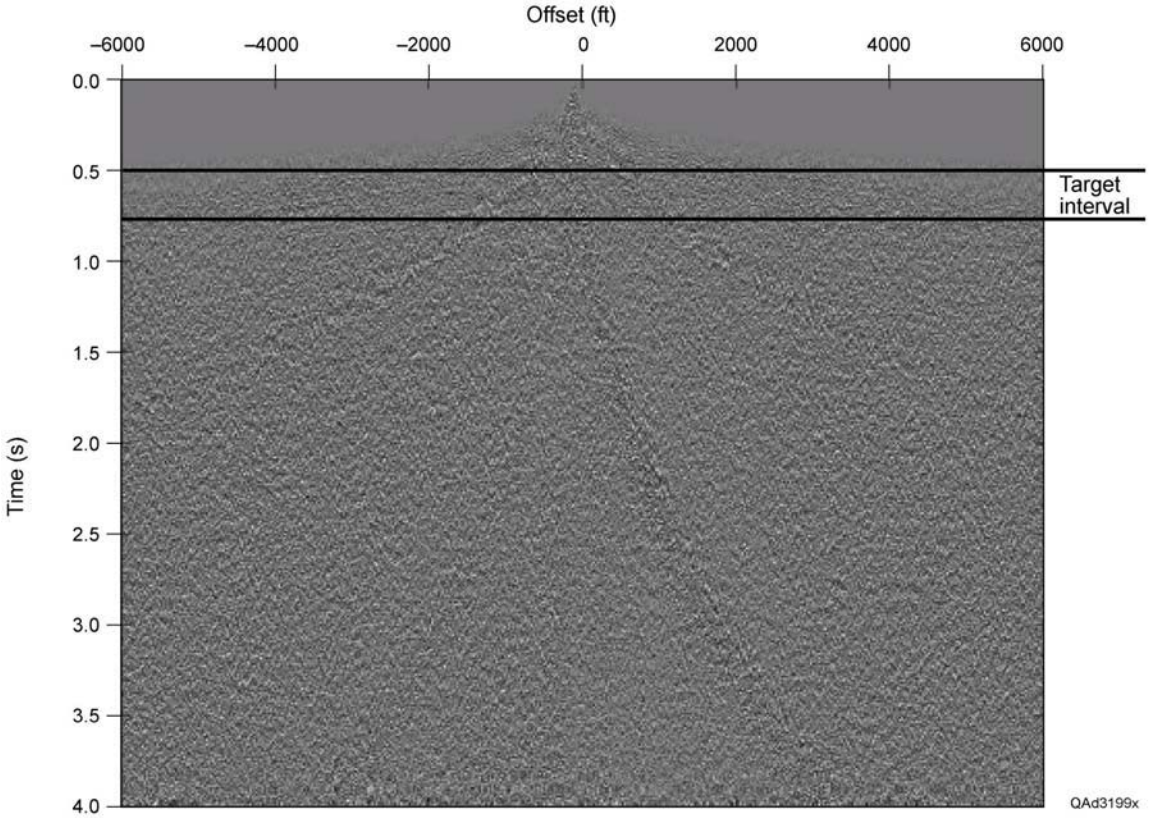

Figure 13. Superbin trace gather of the transverse component of the converted-SV wavefield.

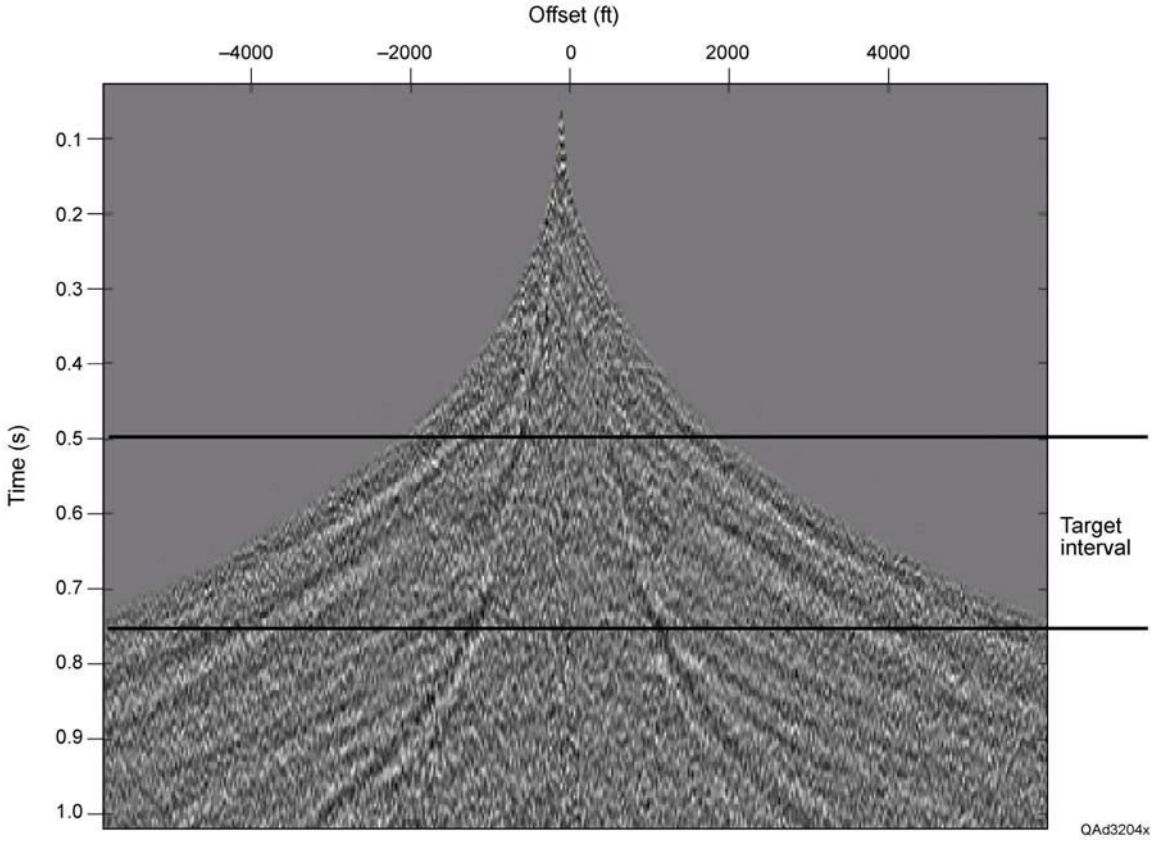

Figure 14. Zoom view of the radial component of the P-SV superbin data illustrating data quality across the reservoir interval.

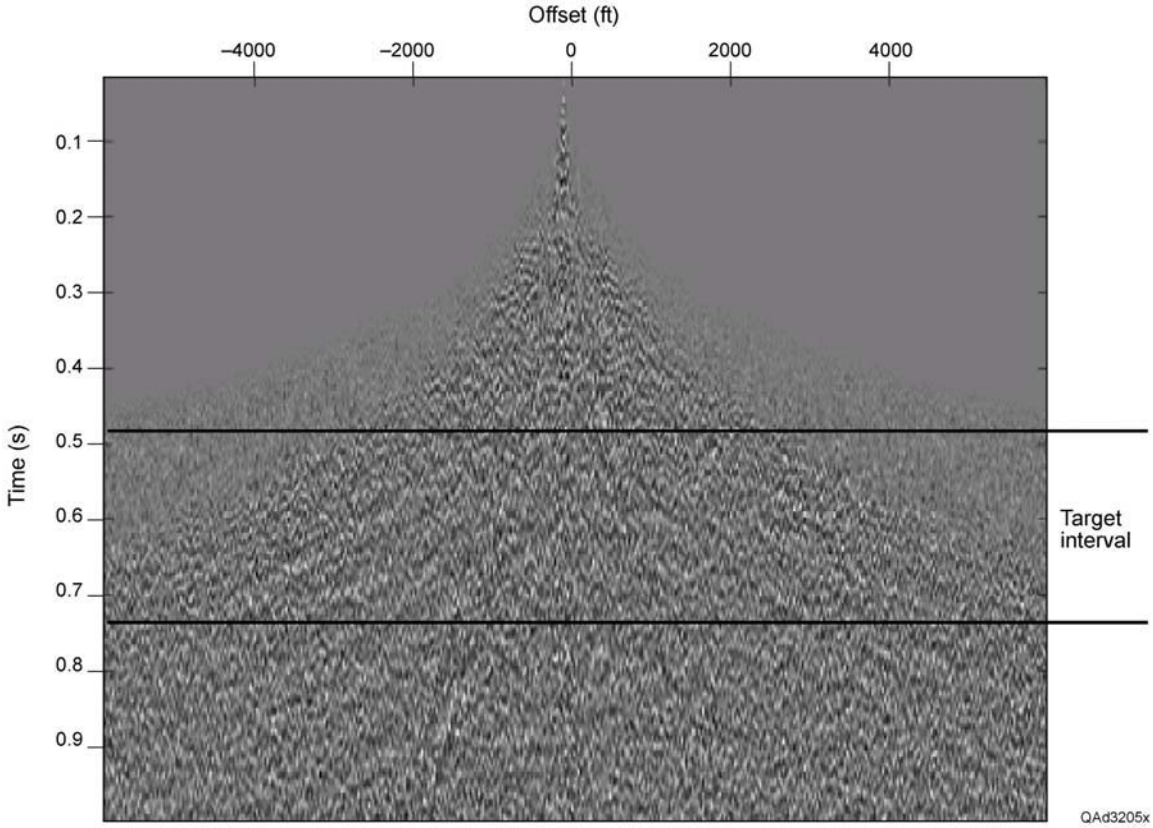

Figure 15. Zoom view of the transverse component of the P-SV superbin data illustrating data quality across the reservoir interval.

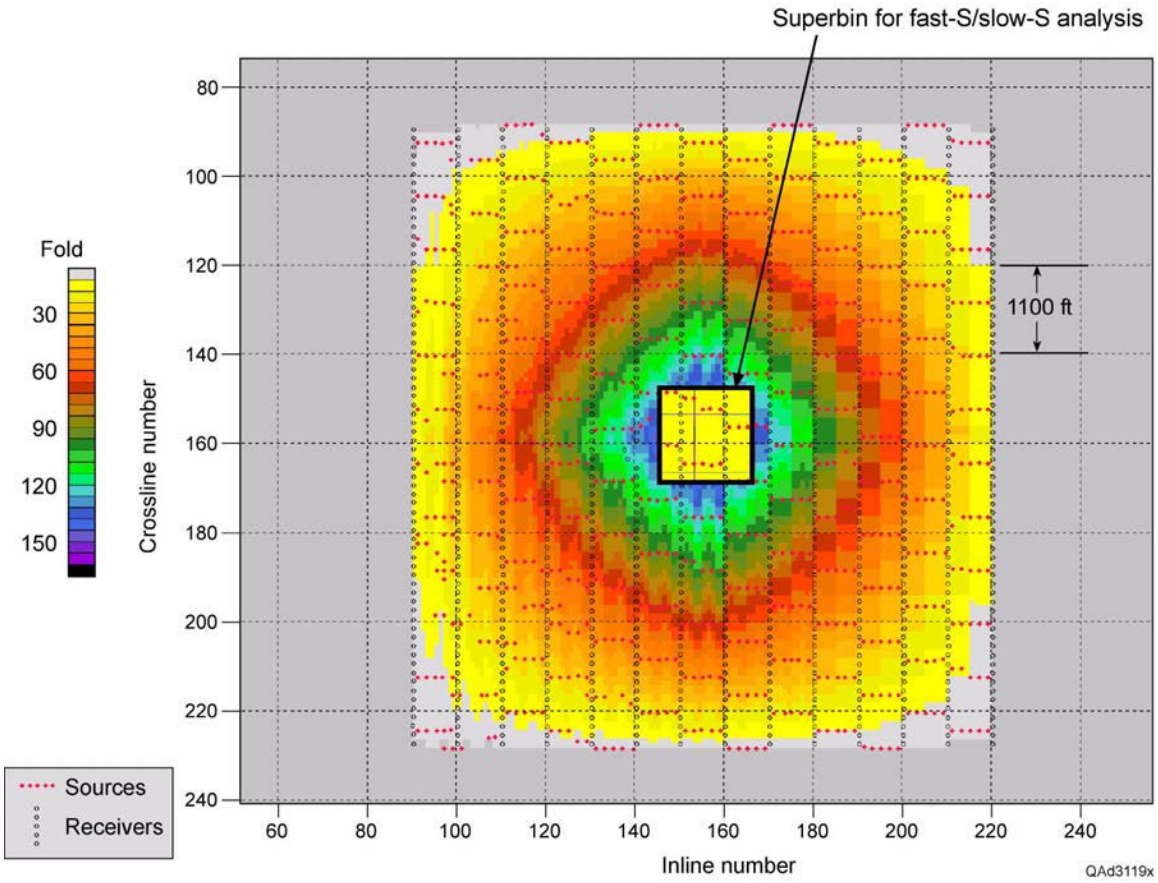

Figure 16. Superbin used to analyze azimuth-dependent properties of P-SV data. The data fold inside the superbin area is approximately 150.

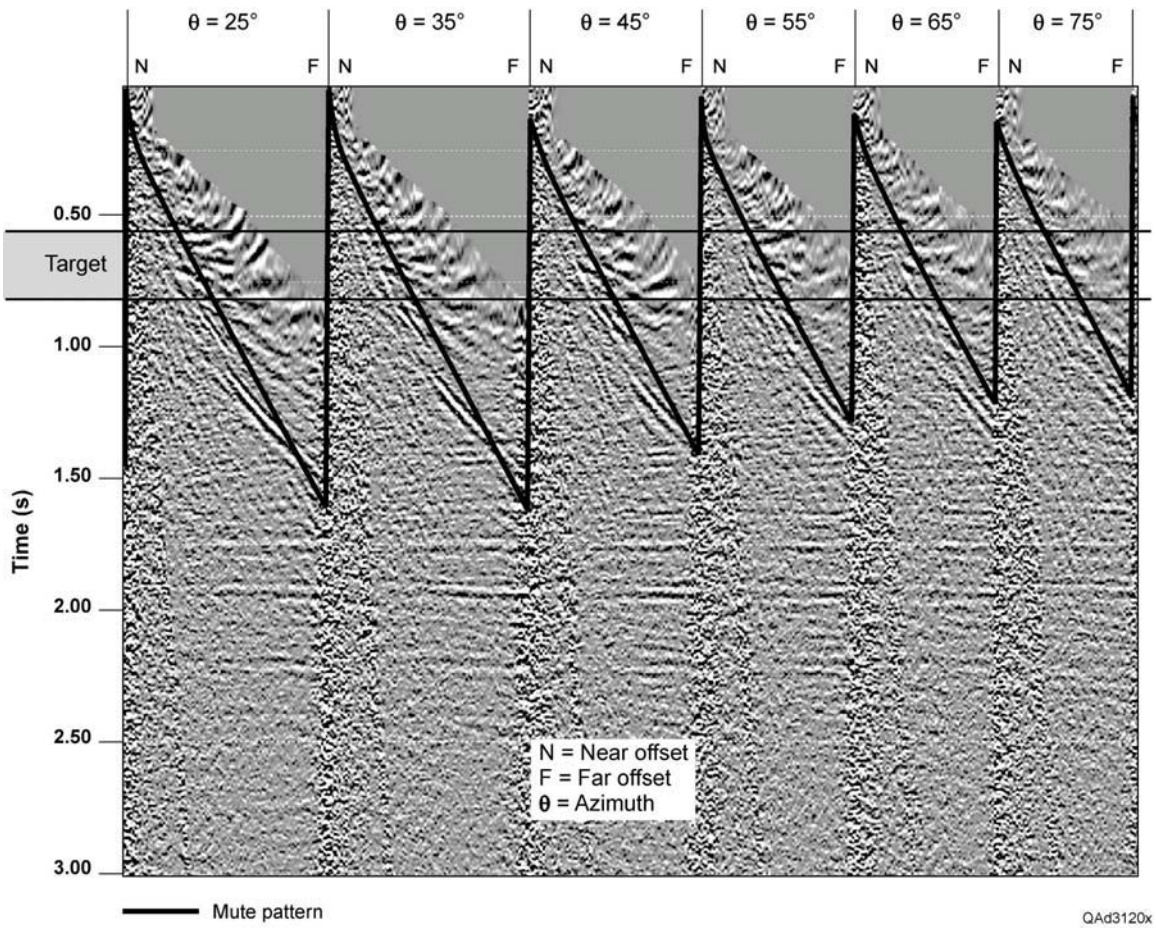

Figure 17. Common-azimuth, radial-component, converted-SV data extracted from the superbin trace gather. The radial component of the P-SV wavefield was segmented into 10-degree azimuth corridors spanning a full azimuth range. The labeled azimuth above each data panel is the midpoint of the 10-degree corridor used to create the trace gather.

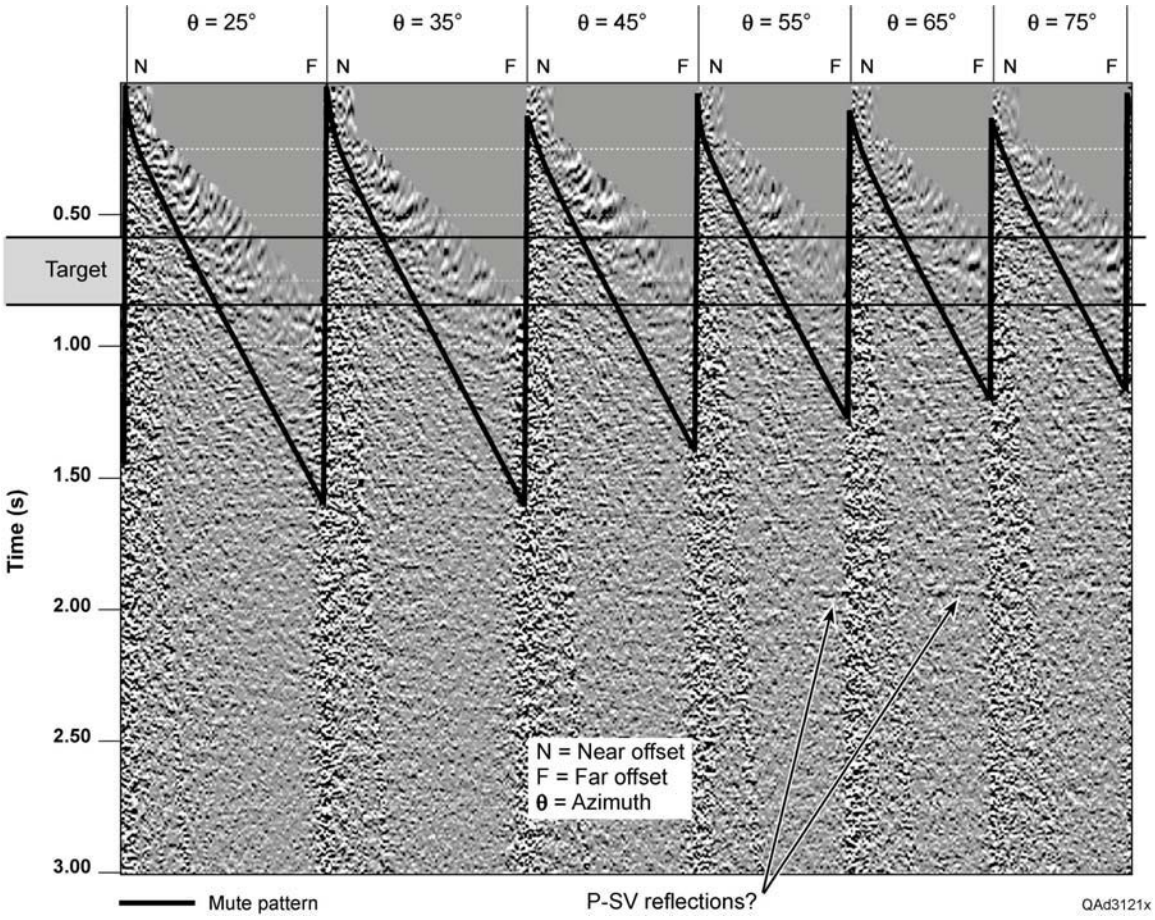

Figure 18. Common-azimuth, transverse-component, converted-SV data extracted from the superbin trace gather. The transverse component of the P-SV wavefield was segmented into 10-degree azimuth corridors spanning a full azimuth range. The labeled azimuth above each data panel is the midpoint of the 10-degree corridor used to create the trace gather.

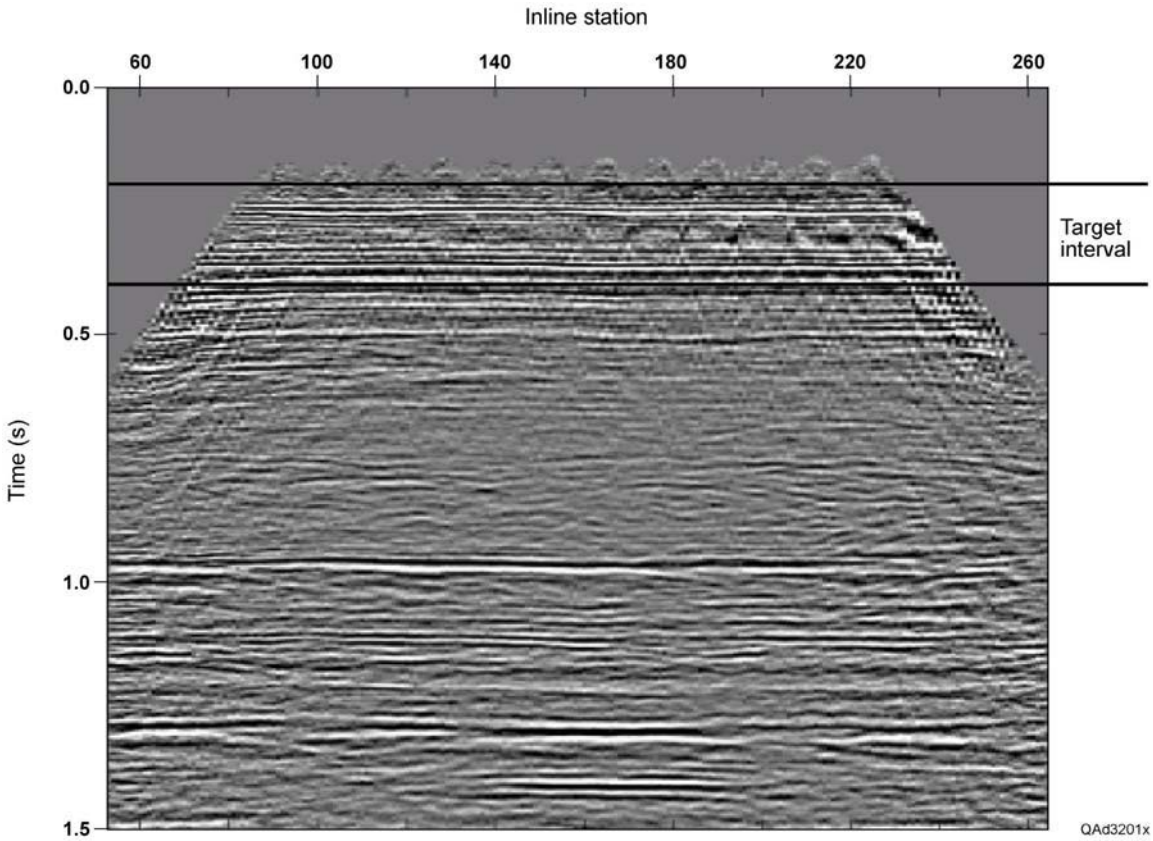

Figure 19. Vertical slice through the stacked P-wave data volume generated from the 3C3D seismic data.

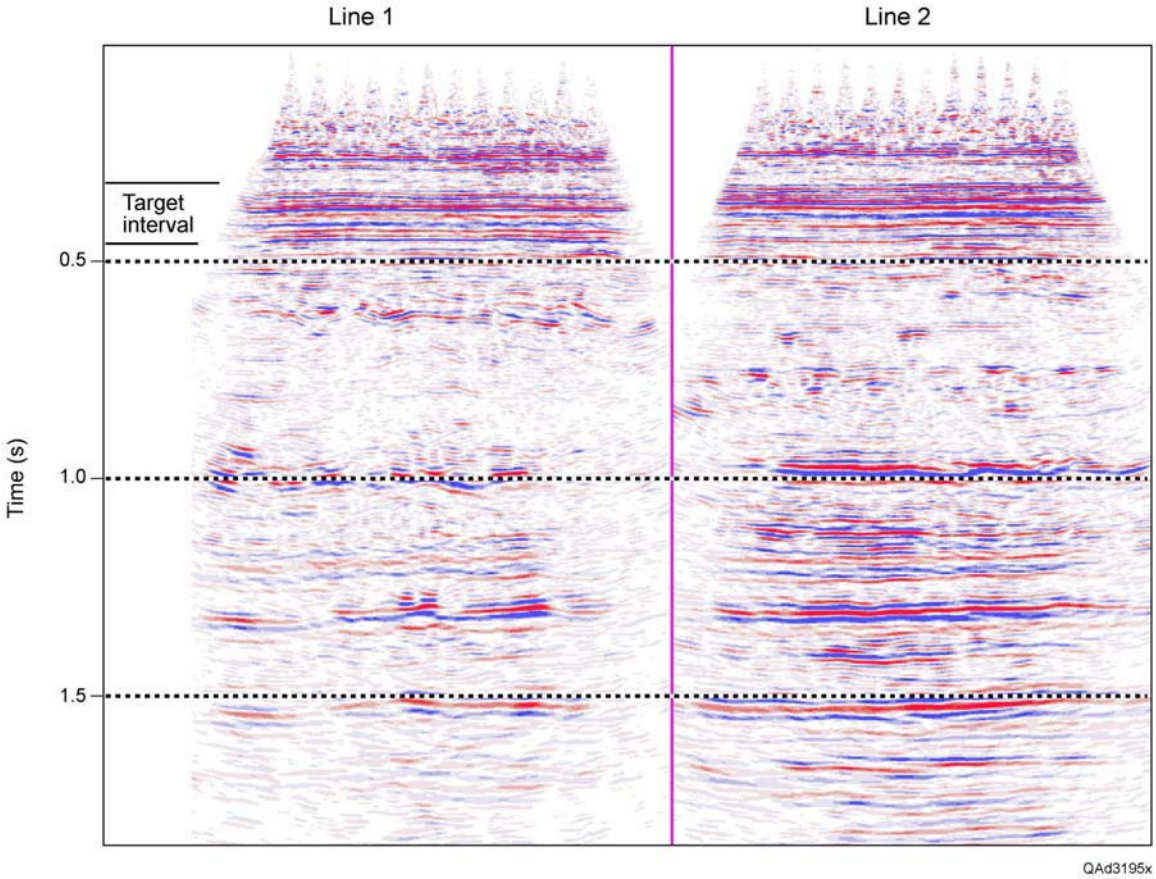

Figure 20. Vertical slices through the migrated P-wave data volume.

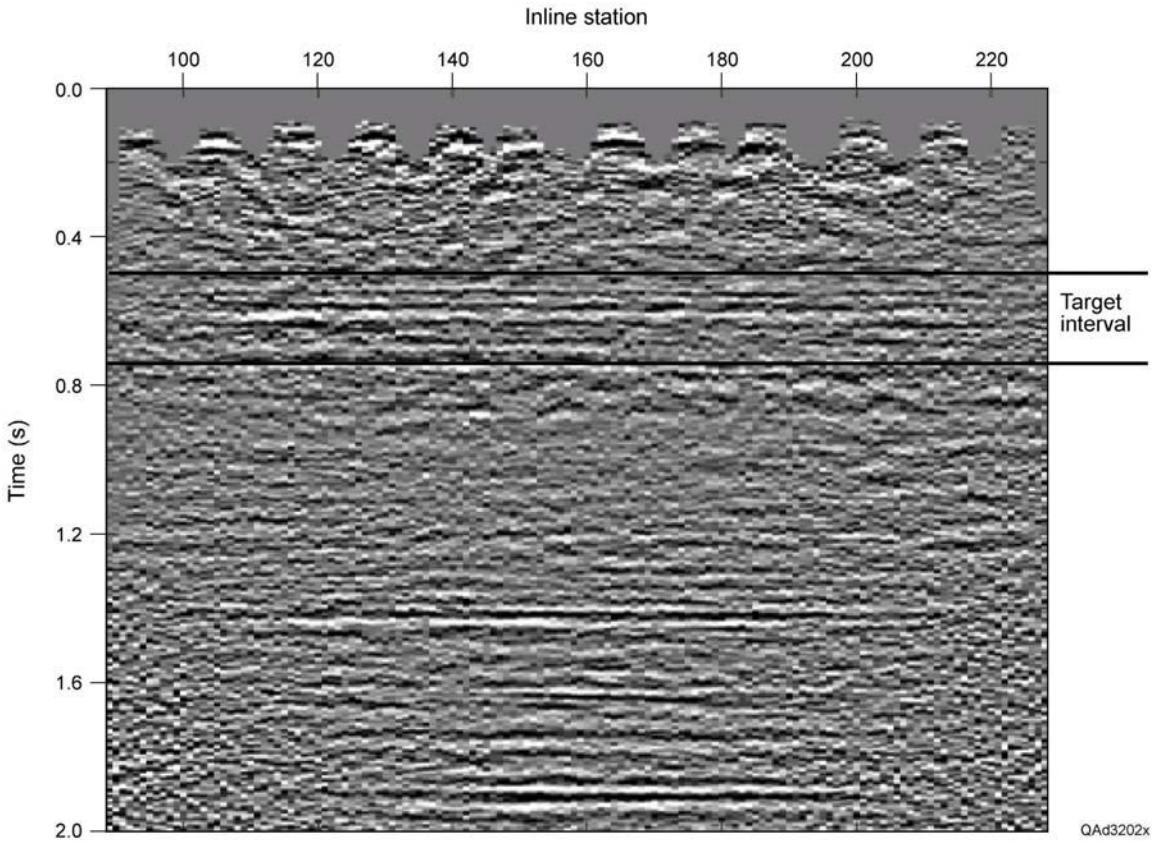

Figure 21. Vertical slice through the stacked volume of radial-component P-SV data.

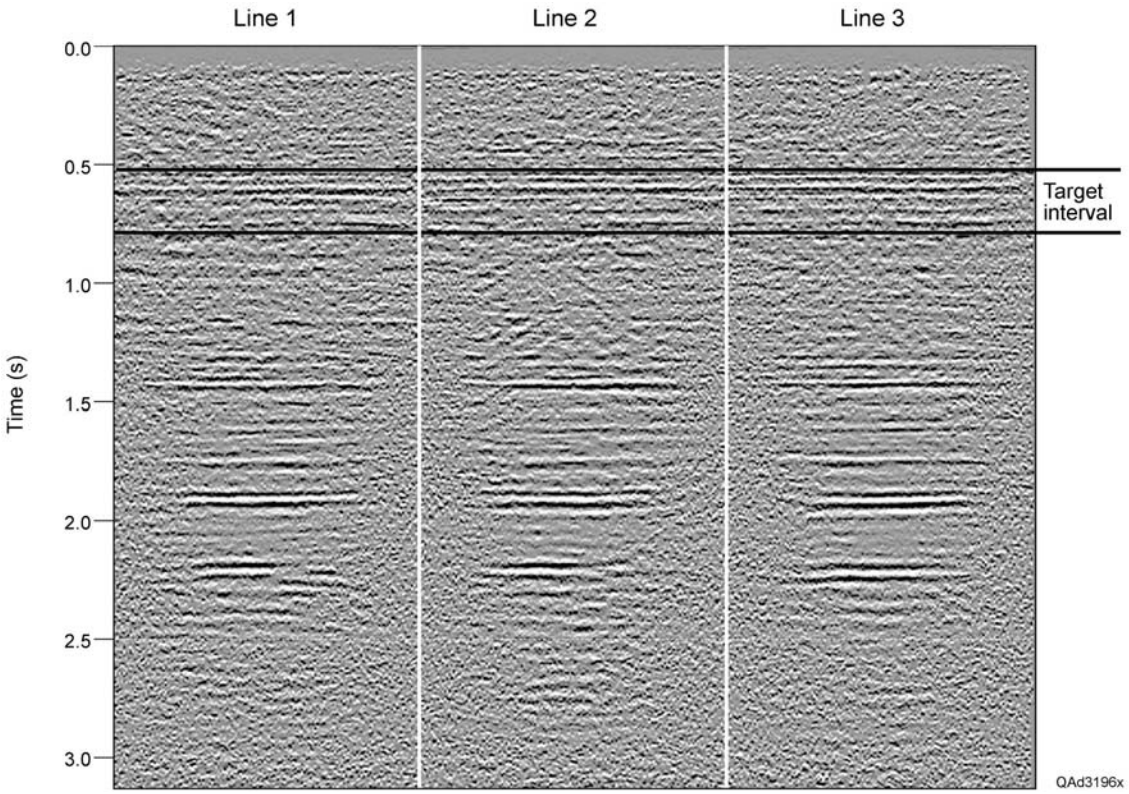

Figure 22. Vertical slices through the migrated volume of radial-component P-SV data.

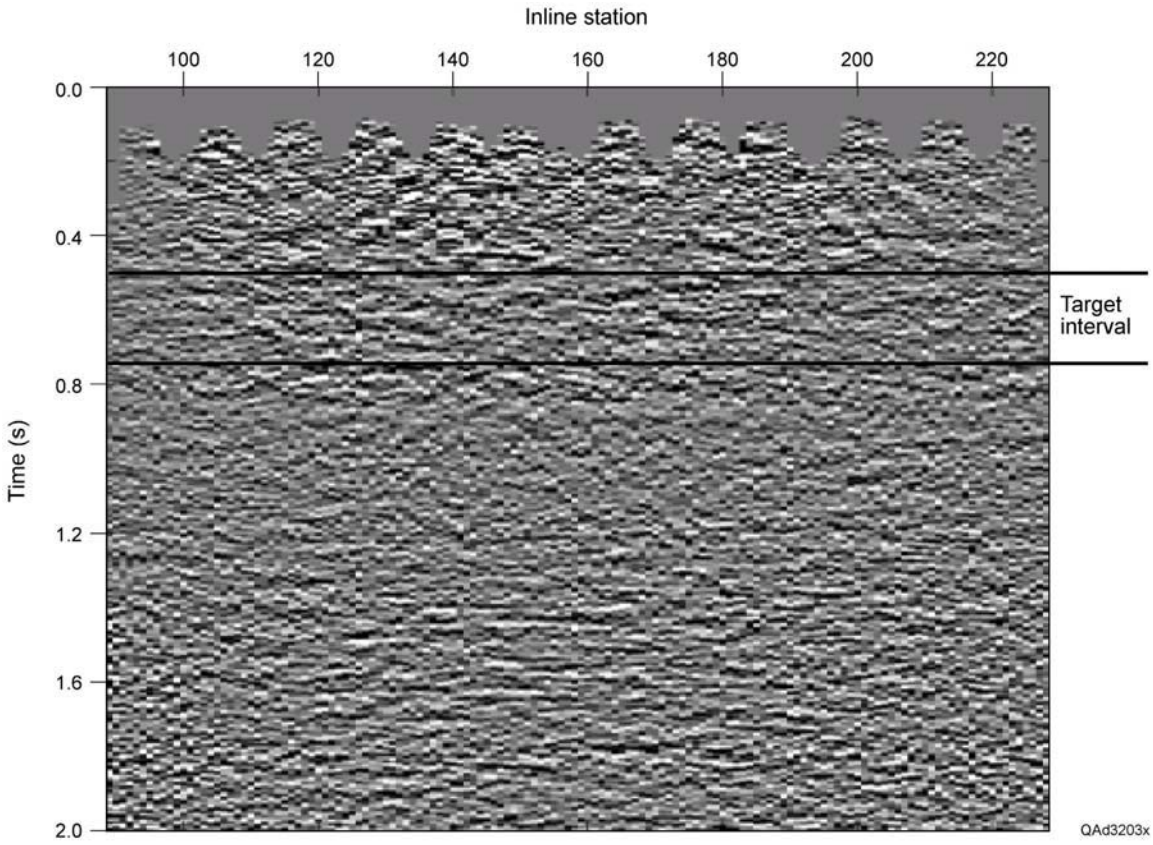

Figure 23. Vertical slice through the stacked volume of transverse-component P-SV data.

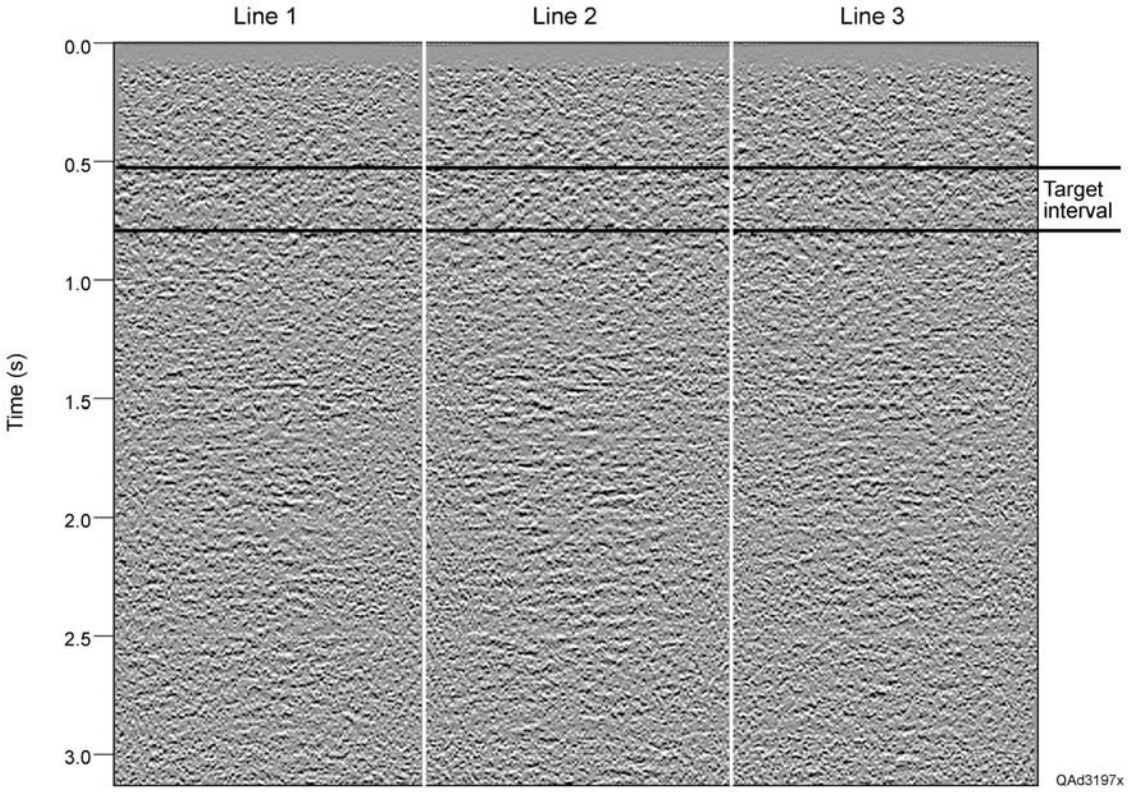

Figure 24. Vertical slices through the migrated volume of transverse-component P-SV data.

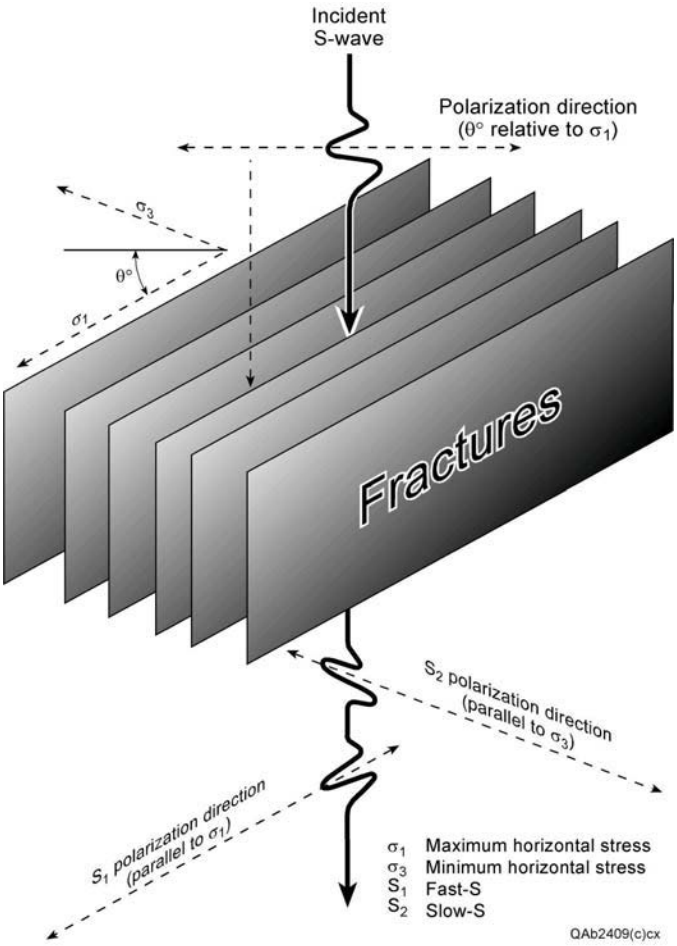

Figure 25. Common model used in geophysical literature to relate S-wave splitting, fracture orientation, and azimuth of maximum horizontal stress

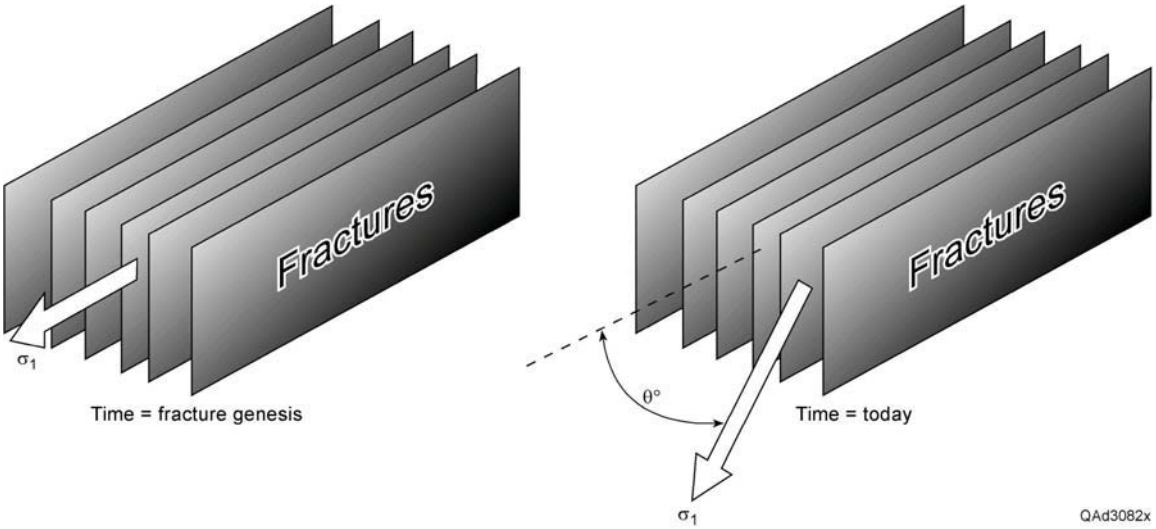

Figure 26. Time-dependent relationships between orientations of extensional fractures and azimuth of maximum horizontal stress.

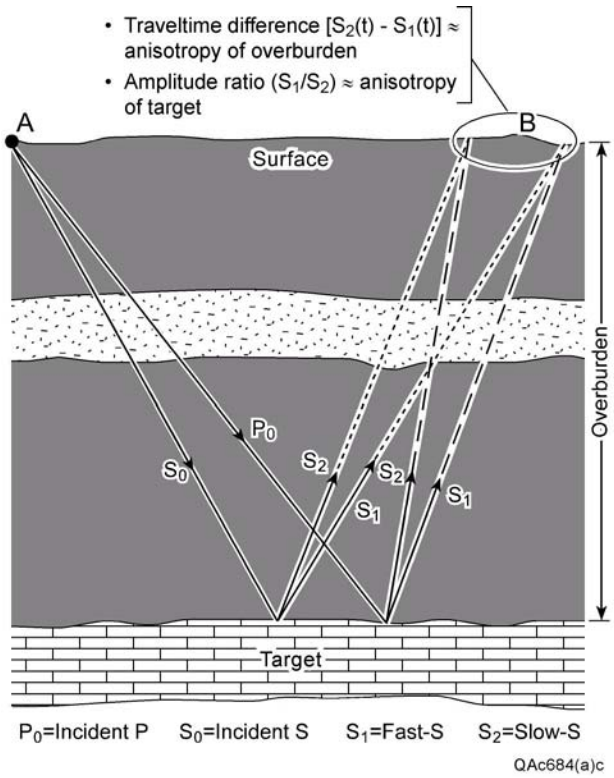

Figure 27. Model illustrating travel paths of S1 and S2 wavelets co-generated at a fracture-zone interface and propagating through a stressed overburden. S1 and S2 polarizations and traveltime differences are controlled by conditions within the overburden, not by the reflection at the fracture target.

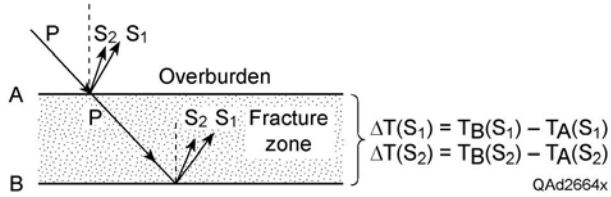

Figure 28. Model illustrating raypaths of S1 and S2 events co-generated at two boundaries A and B that bracket a fractured interval. Interval traveltimes ΔT_1 and $D\Delta_2$ provide information about the fracture space, not information about the overburden.

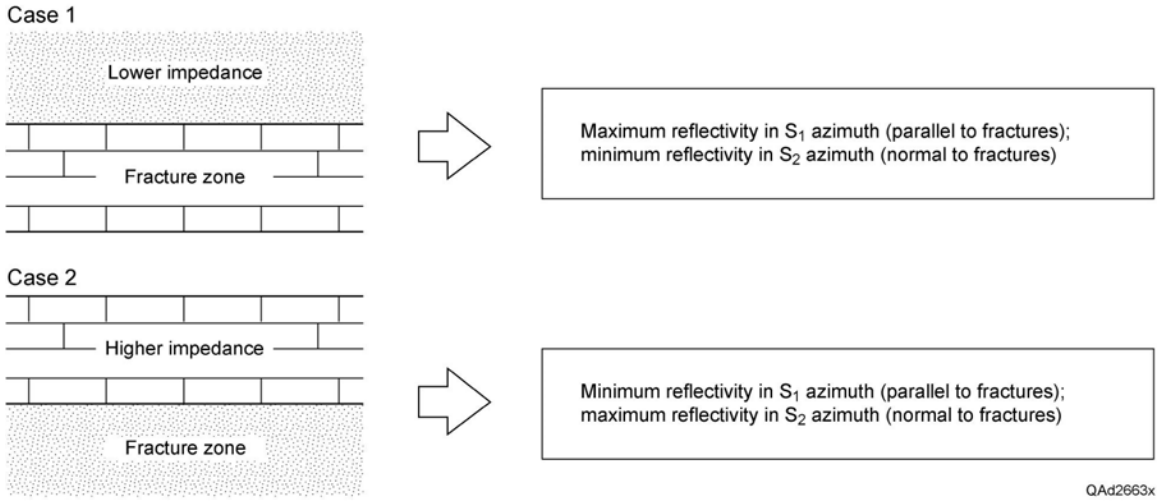

Figure 29. Models summarizing S1 and S2 reflectivities from a fractured target when the overburden has an S-wave impedance less than (Case 1) and greater than (Case 2) the S-wave impedance of the fractured interval.

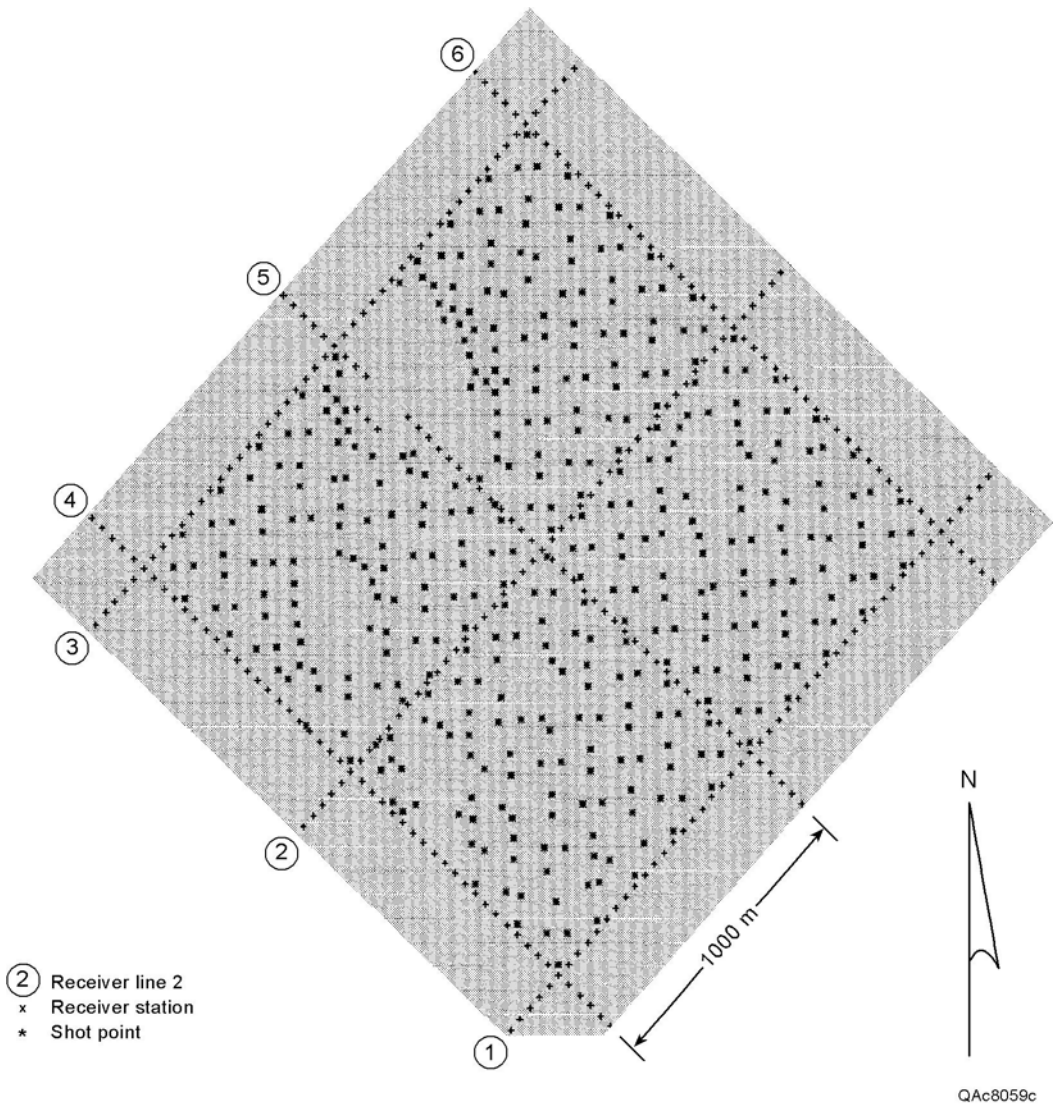

Figure 30. Source-receiver geometry used to acquire 3C3D seismic data across Prospect Number 2.

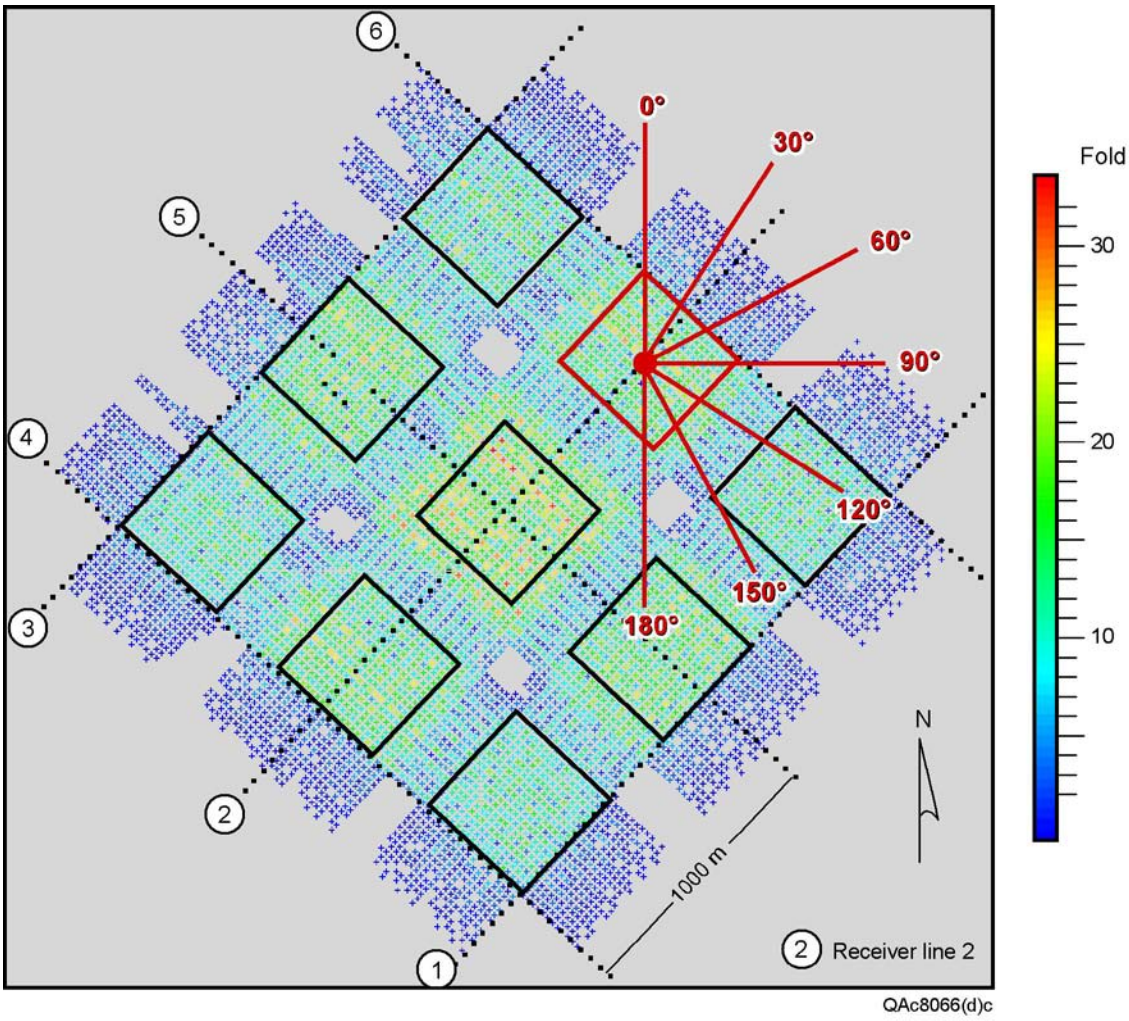

Figure 31. Superbins and azimuth grid used for initial analysis of common-azimuth P-SV trace gathers at Prospect Number 2.

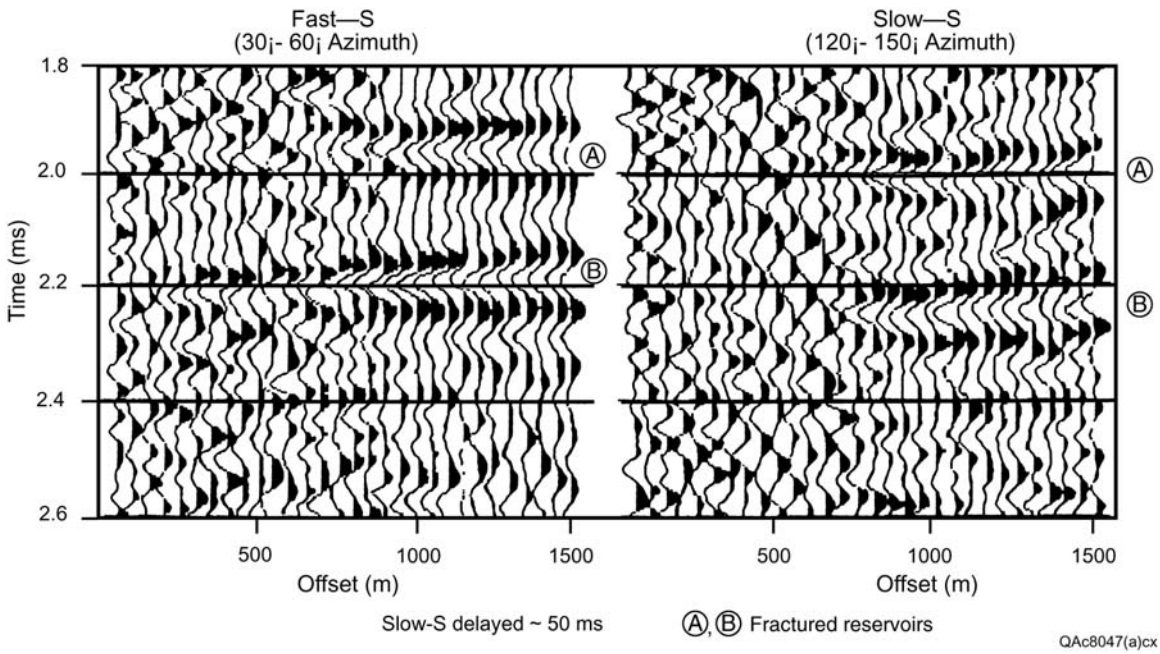

Figure 32. Examples of common-azimuth, radial, P-SV trace gathers constructed at the central superbin location in Figure 31. These data illustrate differences in fast-S and slow-S reflection times in two azimuth directions that differ by 90 degrees. In each trace gather, the azimuth range is limited to 30 degrees.

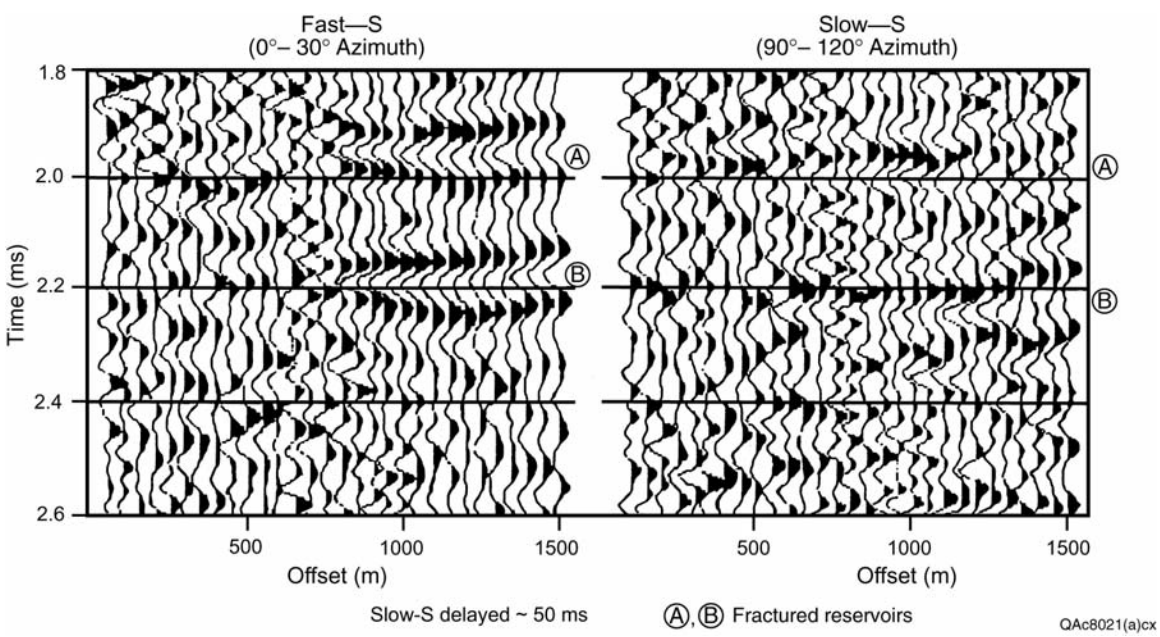

Figure 33. Examples of common-azimuth, radial, P-SV trace gathers constructed at one of the edge superbins in Figure 31. These data show that both P-SV arrival time and P-SV reflectivity vary with azimuth.

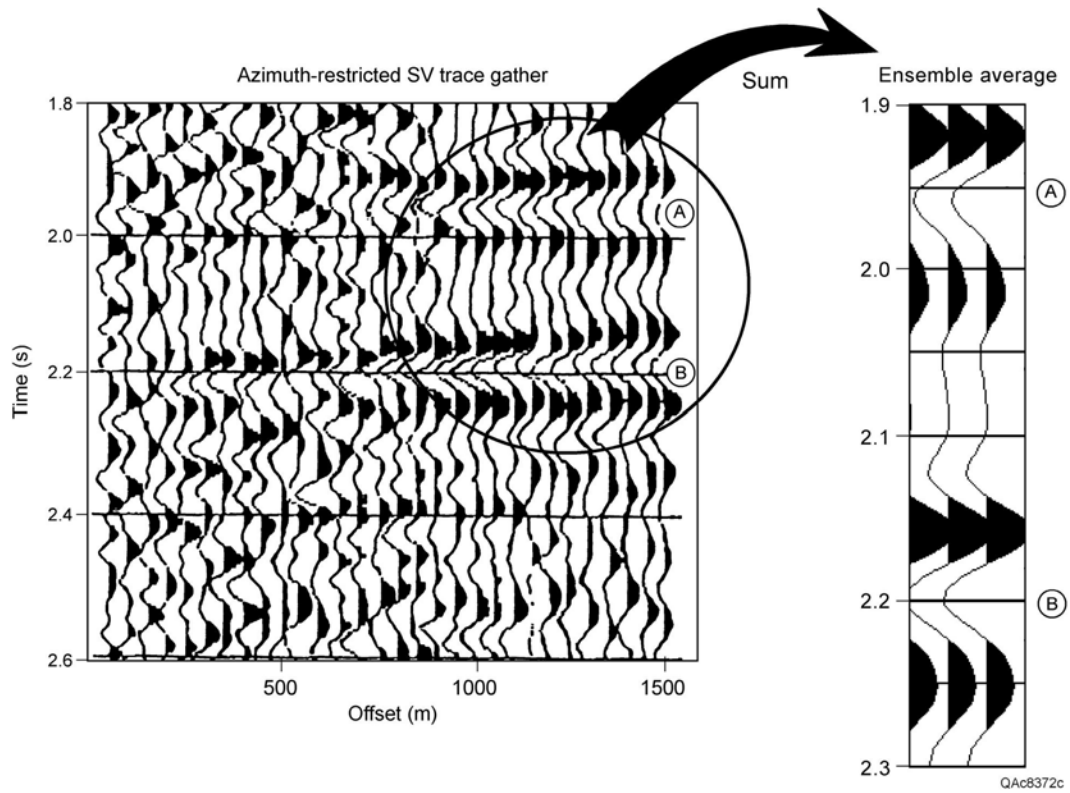

Figure 34. Conversion of a common-azimuth, radial, P-SV trace gather to an ensemble-average trace. The ensemble-average trace is arbitrarily repeated three times to better display its waveshape character.

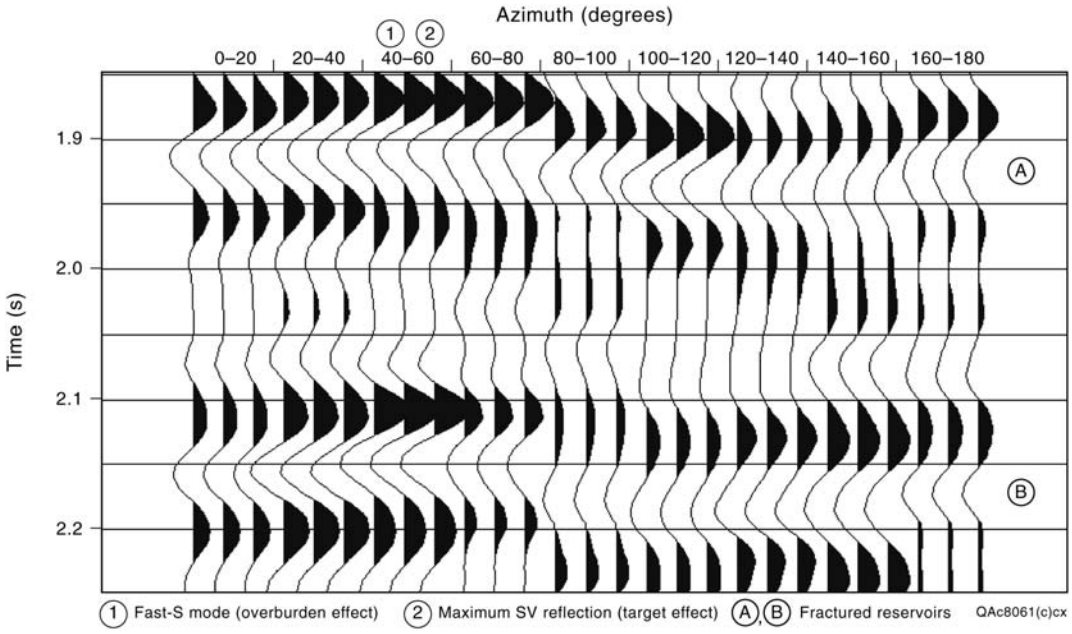

Figure 35. Example of a full-azimuth display of ensemble-average traces constructed at a centrally located, but smaller superbin. These data are the radial component of the P-SV wavefield. The azimuth range of 20 degrees used here was used in all subsequent data analyses.

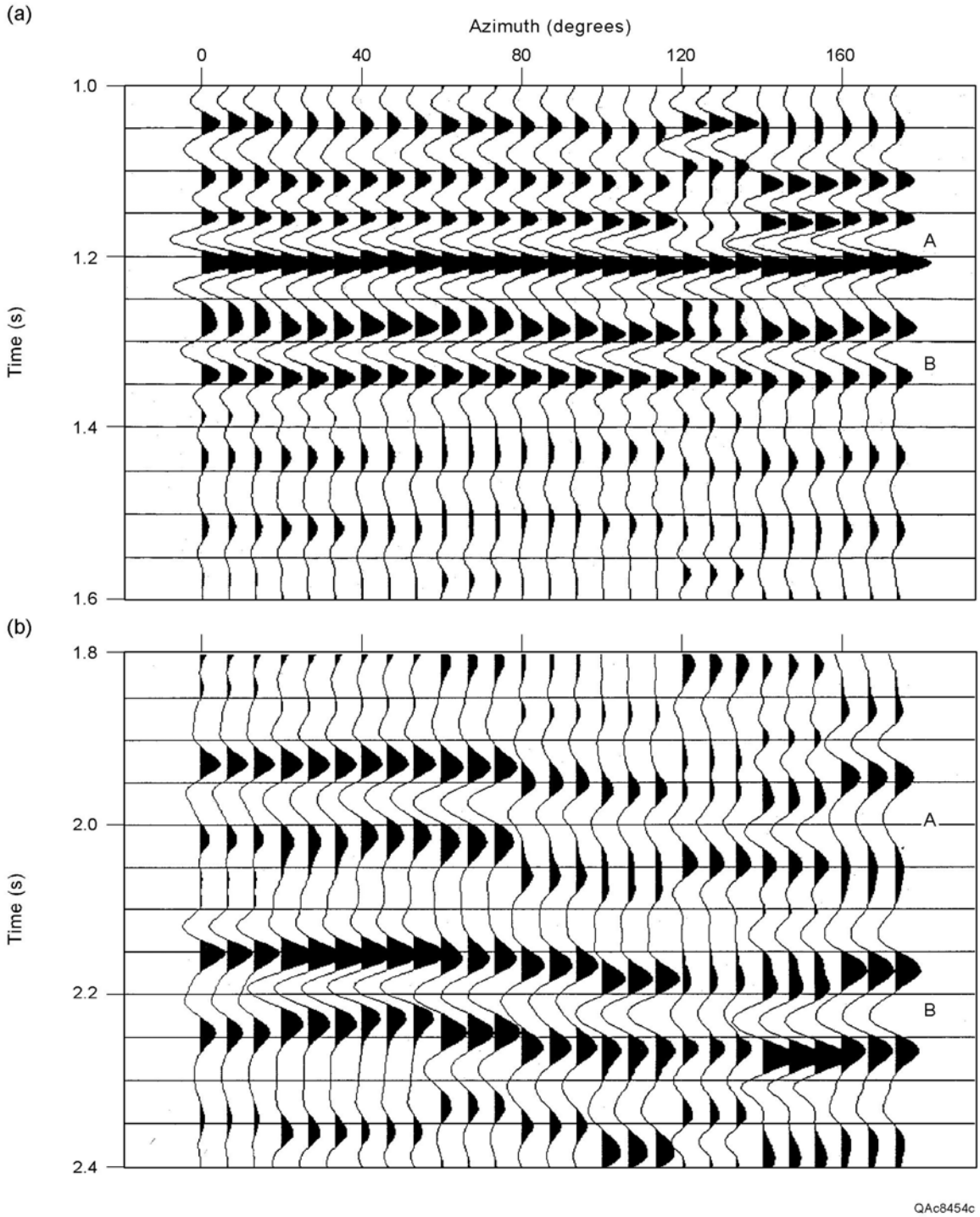

Figure 36. Typical low azimuth sensitivity of P-P reflection time and amplitude observed across Prospect Number 2 (top). Converted-SV data exhibit much stronger azimuth variations in velocity and reflectivity at the same location (bottom).

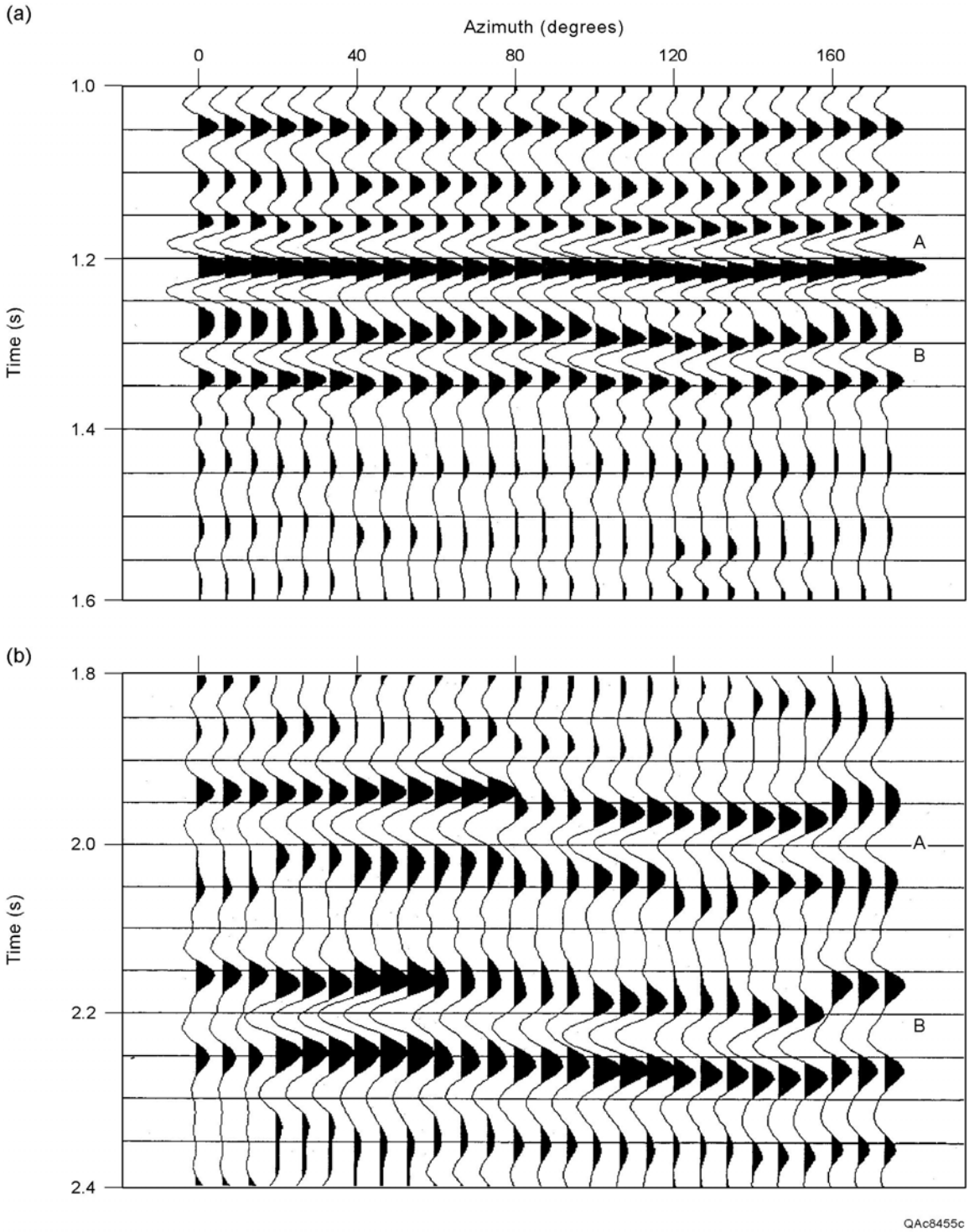

Figure 37. The largest magnitude of P-P azimuth-dependent velocity behavior observed across the study area (top). P-SV azimuth-dependent velocity and reflectivity at the same location (bottom).

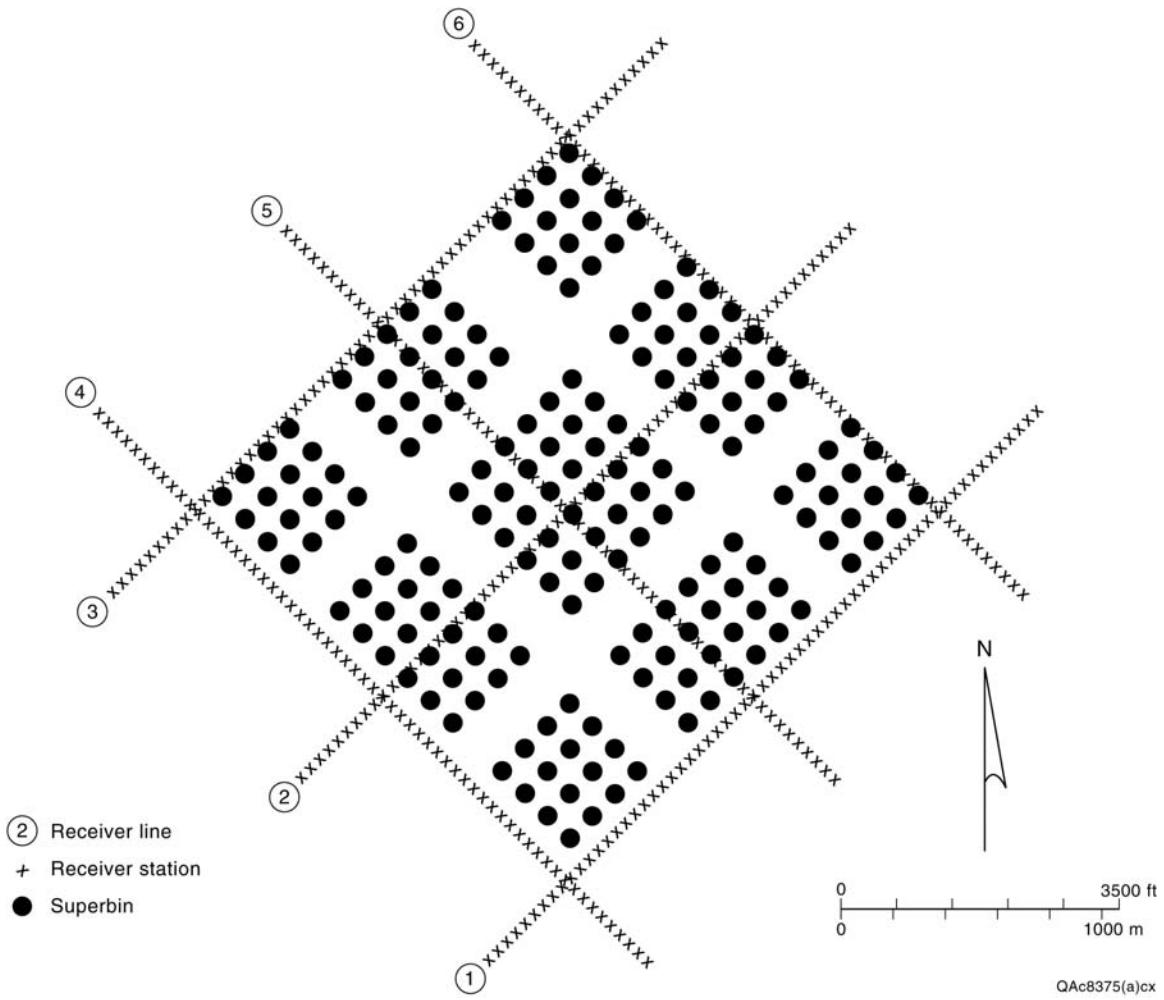

Figure 38. Superbin analysis sites across Prospect Number 2. Each superbin consisted of 9 × 9 standard bins. Adjacent superbins had a 4-bin overlap.

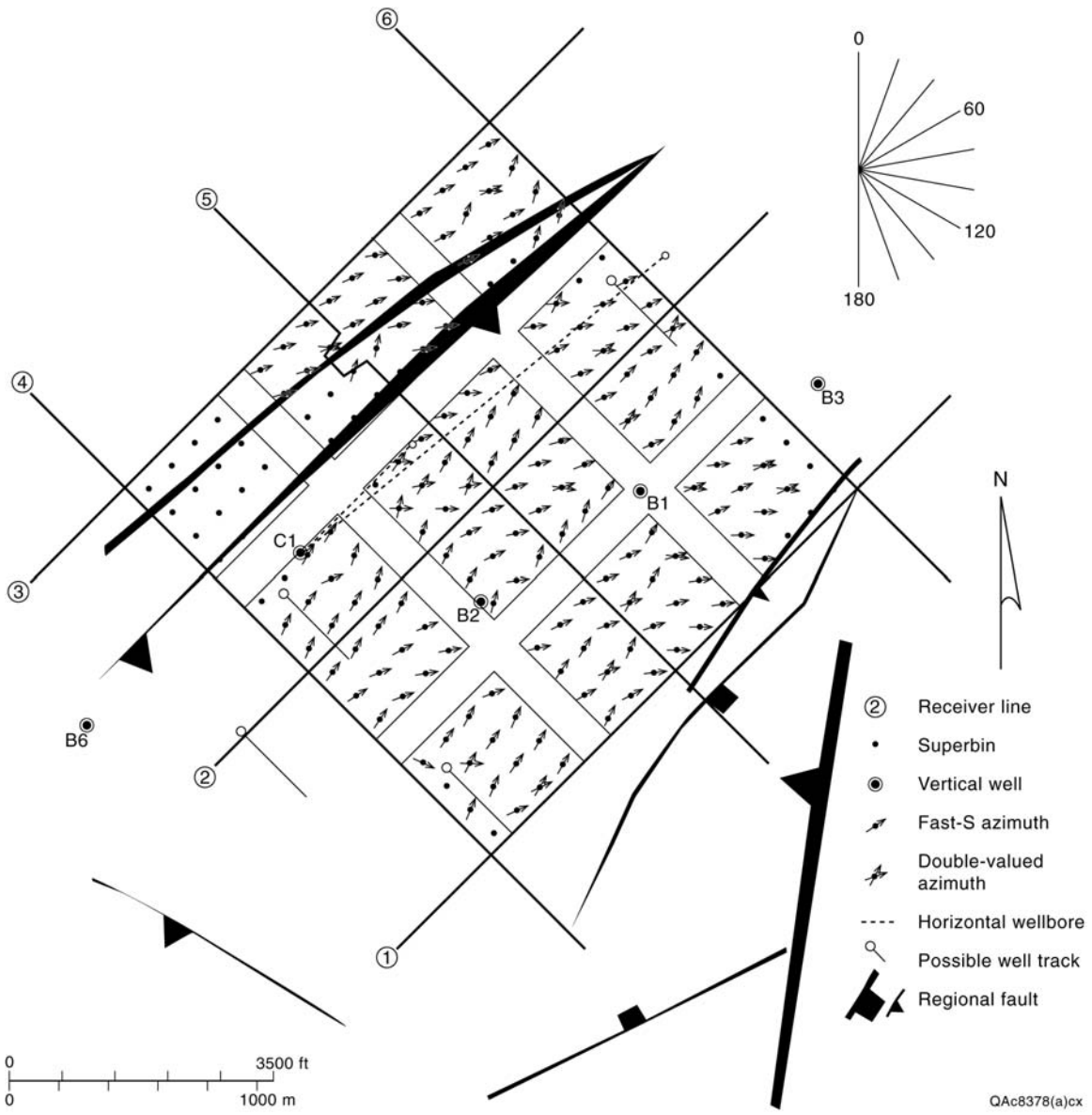

Figure 39. Map of fast-S azimuth at Prospect Number 2. The S1 polarization direction at each superbin location was assumed to define the azimuth orientation of the maximum horizontal stress acting in the overburden above the fractured reservoirs at the X,Y coordinates of the superbin.

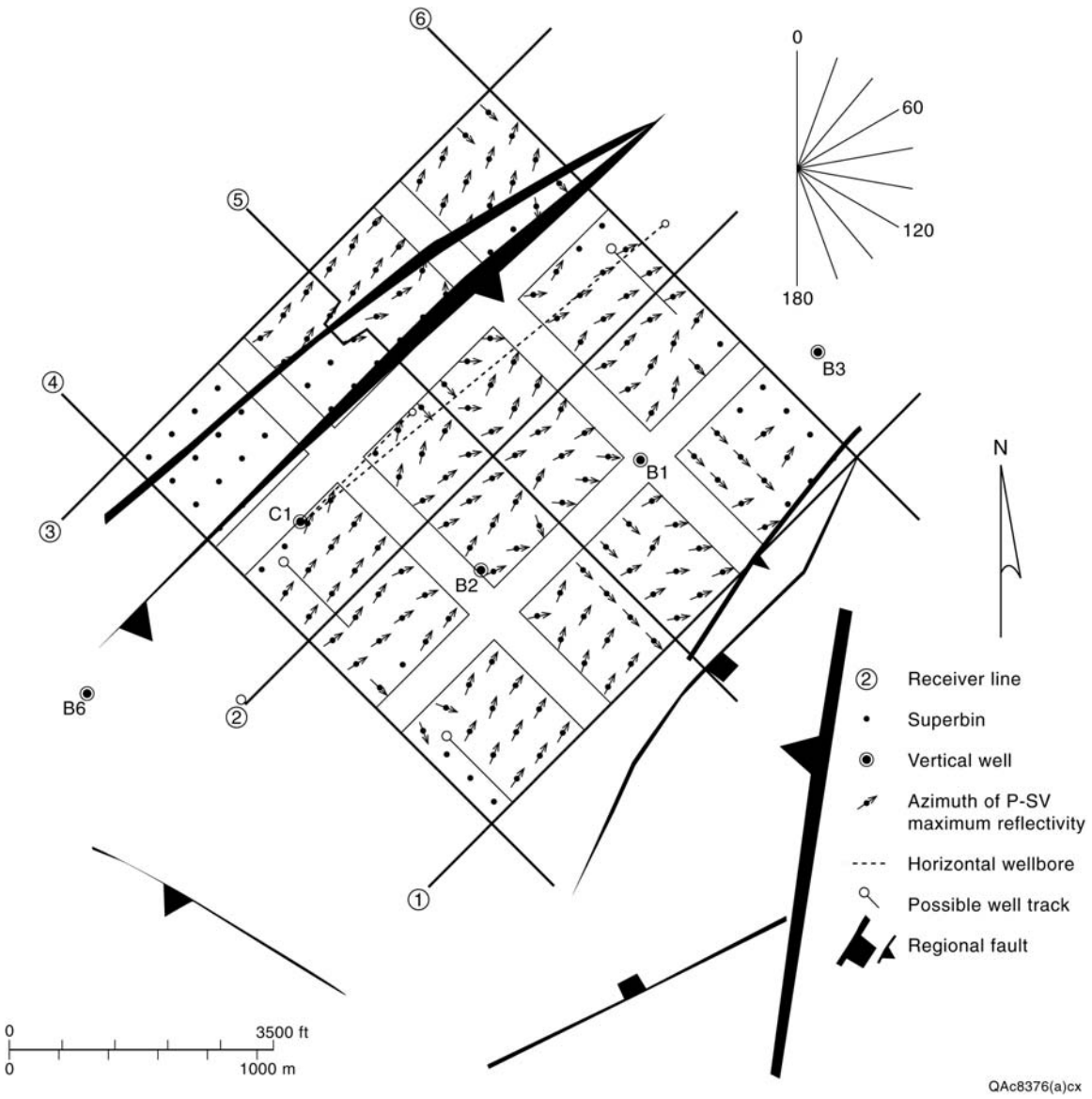

Figure 40. Azimuths of P-SV maximum reflectivity for Reservoir A across Prospect Number 2. These azimuth arrows are assumed to align with the near-vertical fractures in this upper reservoir (A).

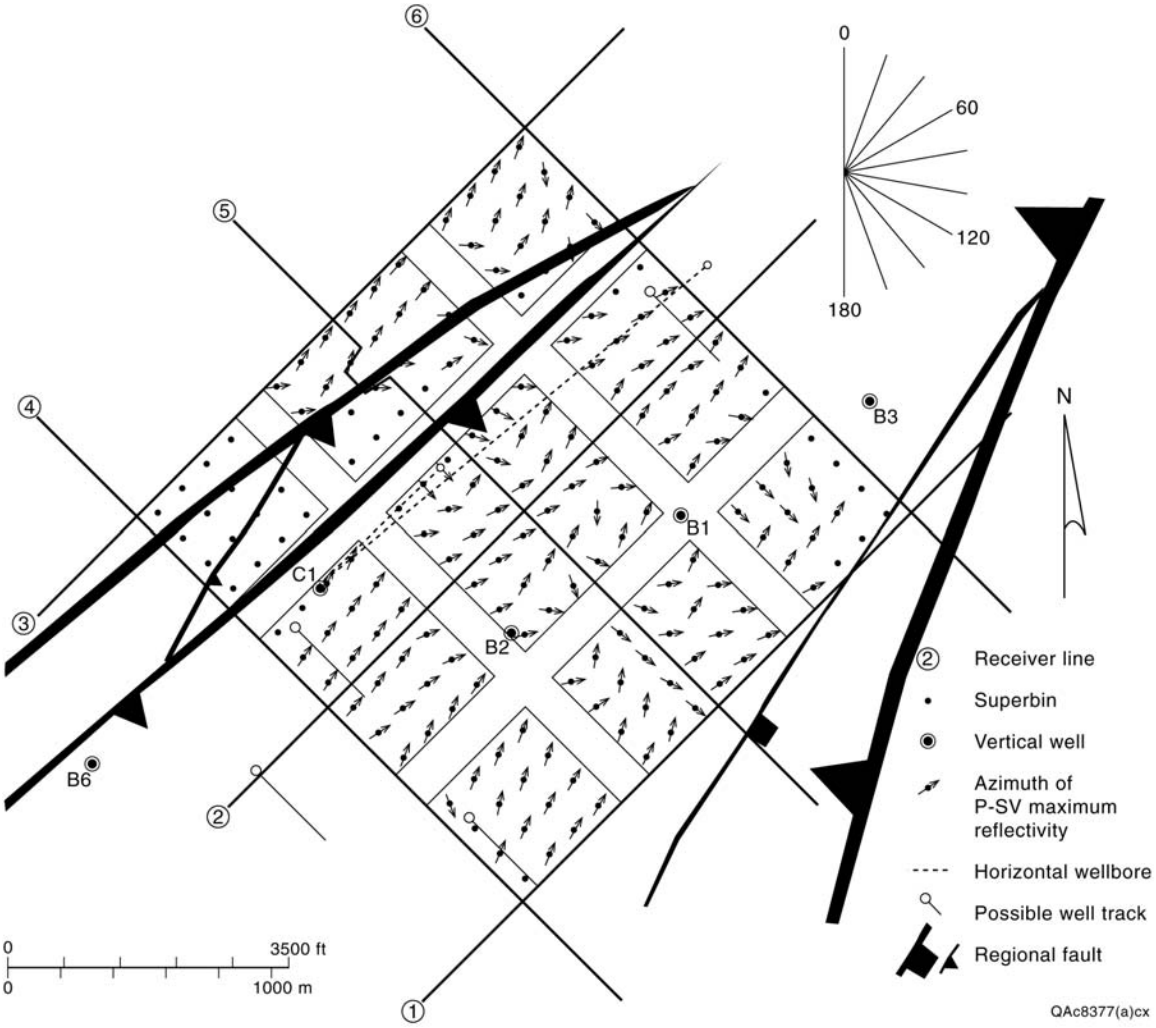

Figure 41. Azimuths of P-SV maximum reflectivity for Reservoir B across Prospect Number 2. The azimuths differ from the azimuths estimated for Reservoir A at only a few superbins, implying similar orientations of near-vertical fractures occur in both reservoirs.

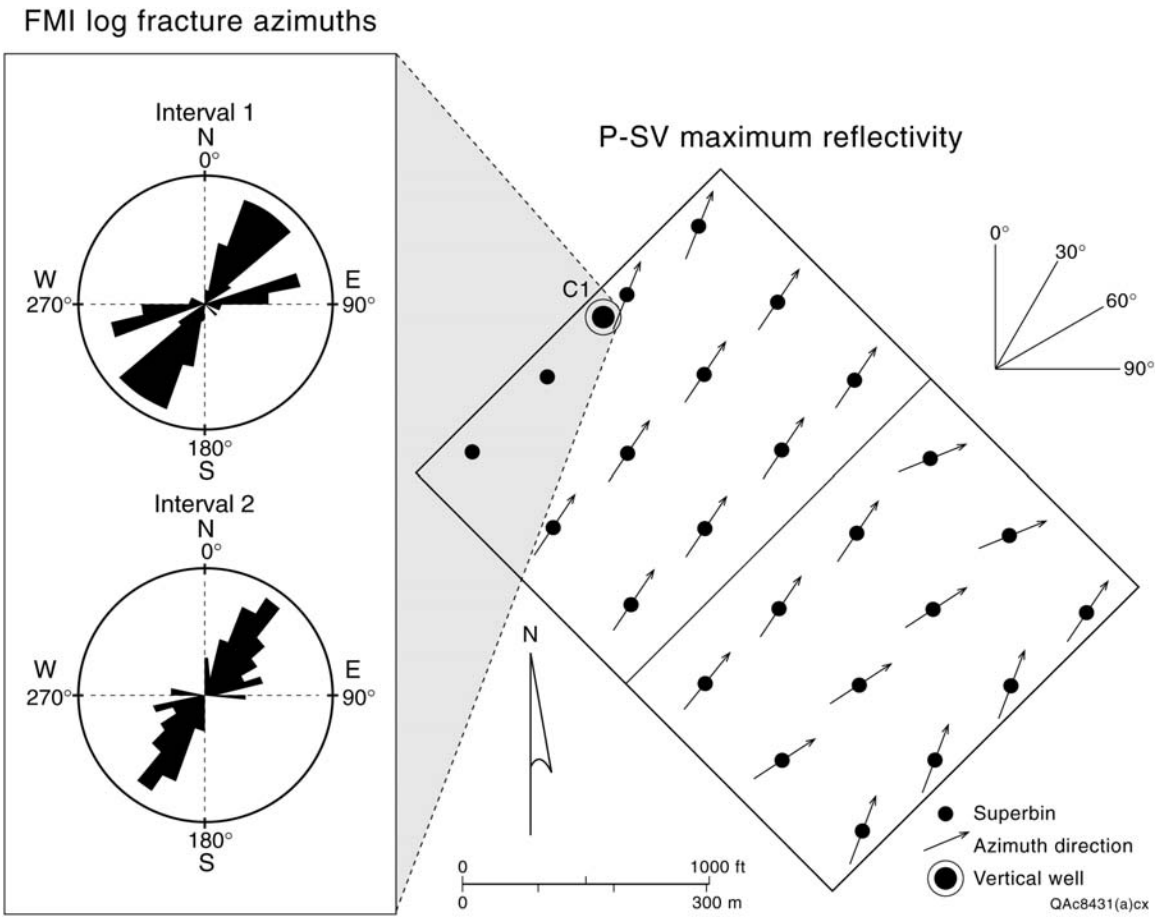

Figure 42. Comparison of FMI-based and seismic-based estimations of near-vertical fracture azimuths, Reservoir B, Prospect Number 2.

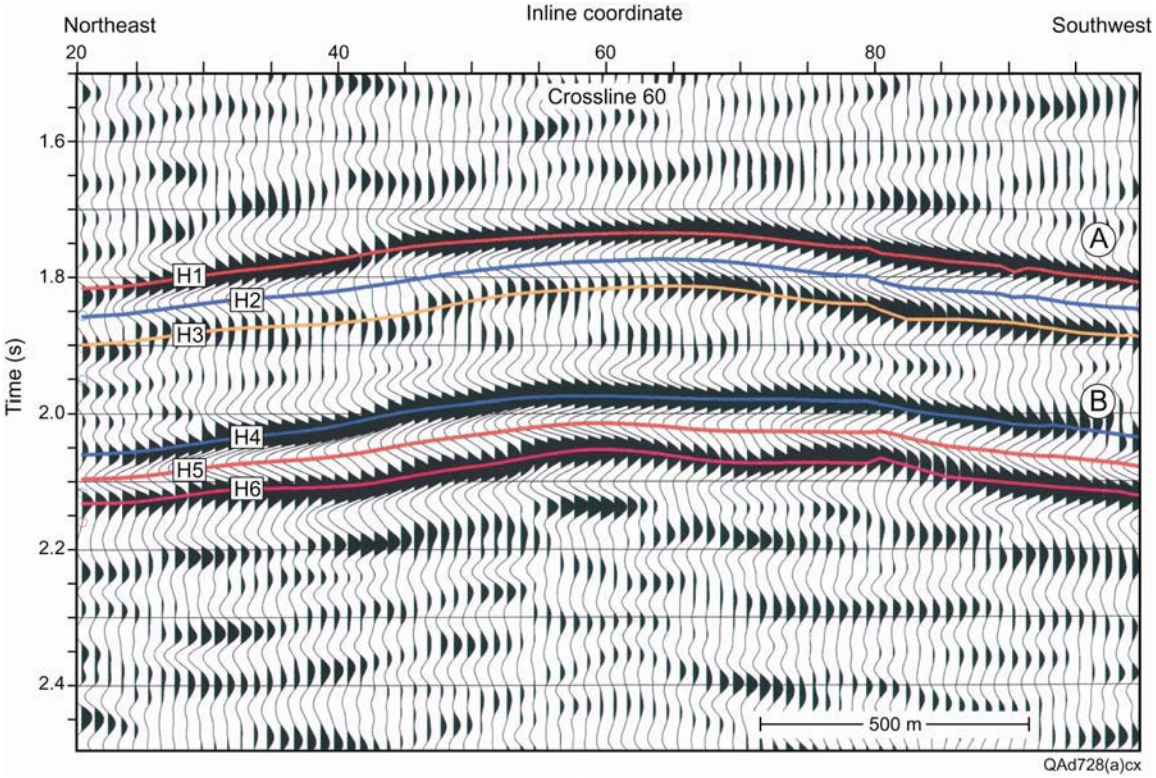

Figure 43. Crossline 60 through S1 data volume at Prospect Number 2.

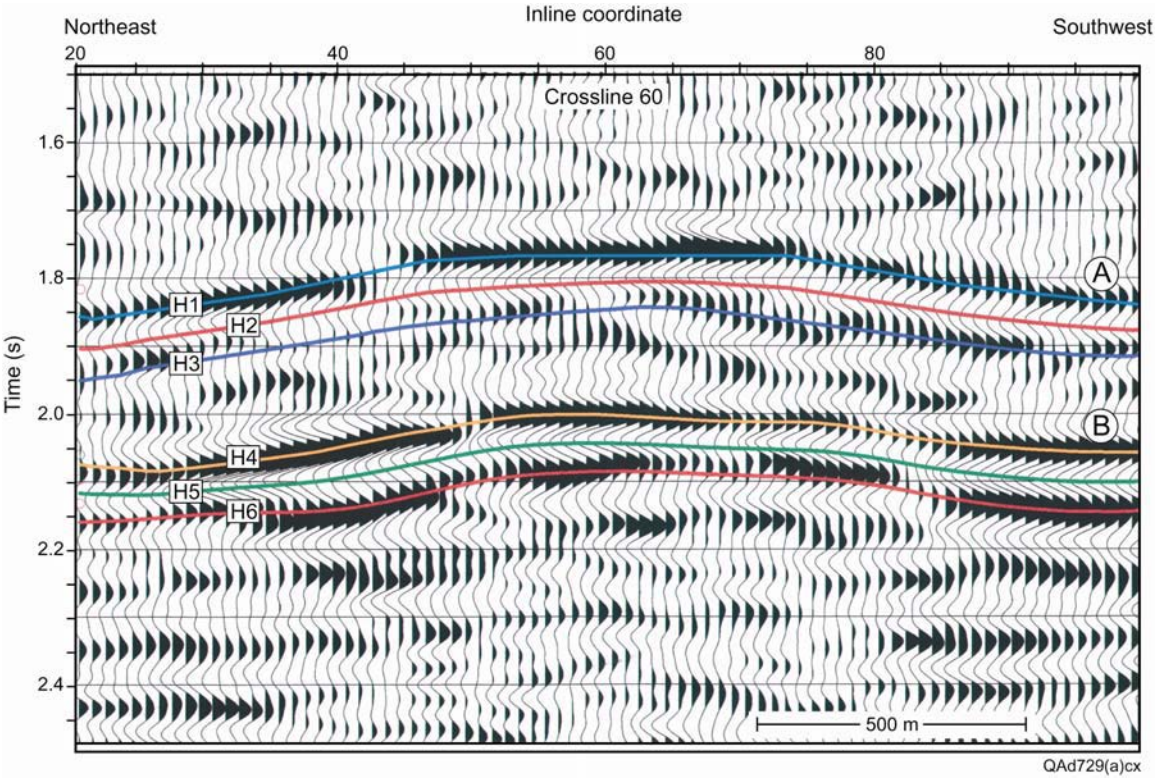

Figure 44. Crossline 60 through S2 data volume at Prospect Number 2.

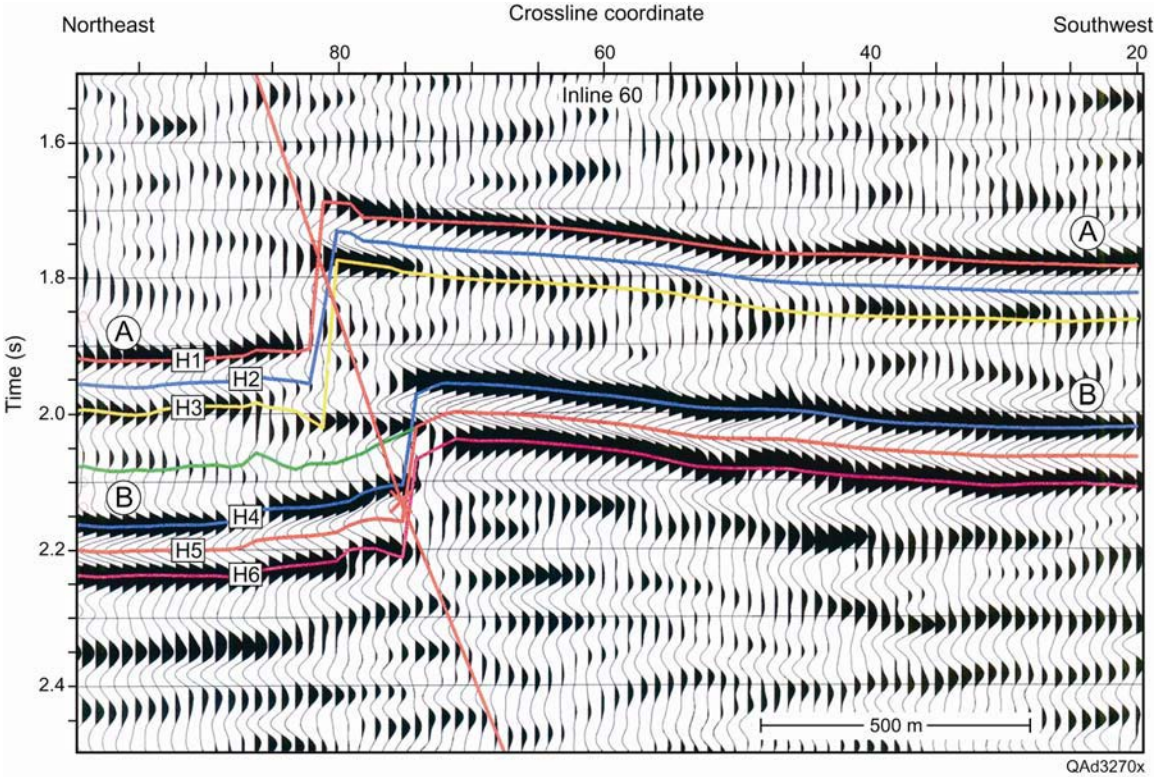

Figure 45. Inline 60 through S1 data volume at Prospect Number 2.

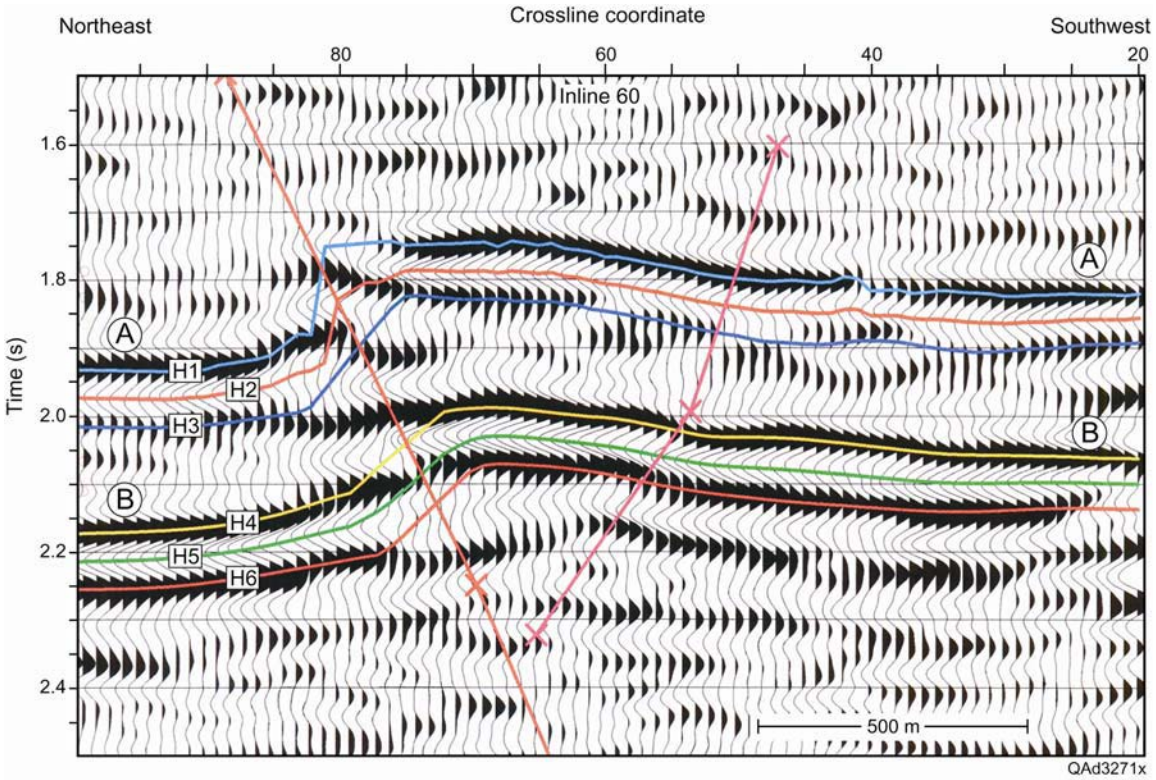

Figure 46. Inline 60 through S2 data volume at Prospect Number 2.

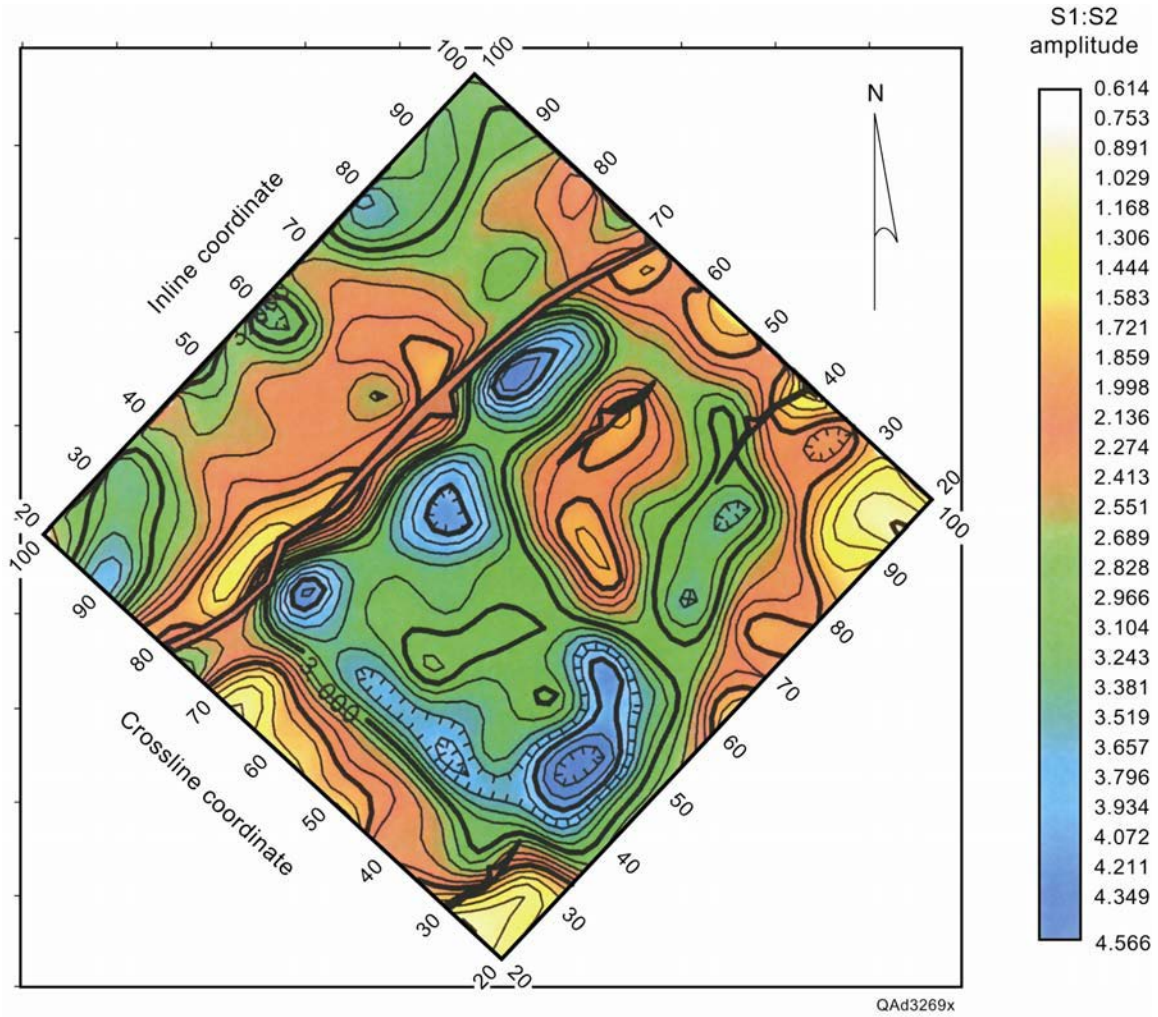

Figure 47. Map of S1-to-S2 reflection amplitudes (rms) from Reservoir B, Prospect Number 2. Higher ratios are interpreted as indications of increased fracture content with the interval spanning Reservoir B.